

Atmospheric composition and circulation of the ultra-hot Jupiter WASP-121b with joint NIRPS, HARPS and CRIRES+ transit spectroscopy

Valentina Vaulato^{1,*}, Melissa J. Hobson¹, Romain Allart², Stefan Pelletier^{1,2}, Joost P. Wardenier², Hritam Chakraborty¹, David Ehrenreich^{1,3}, Nicola Nari^{4,5,6}, Michal Steiner¹, Xavier Dumusque¹, H. Jens Hoeijmakers⁷, Étienne Artigau^{2,8}, Frédérique Baron^{2,8}, Susana C. C. Barros^{9,10}, Björn Benneke^{11,2}, Xavier Bonfils¹², François Bouchy¹, Marta Bryan¹³, Bruno L. Canto Martins¹⁴, Ryan Cloutier¹⁵, Neil J. Cook², Nicolas B. Cowan^{16,17}, Jose Renan De Medeiros¹⁴, Xavier Delfosse¹², Elisa Delgado-Mena^{18,9}, René Doyon^{2,8}, Jonay I. González Hernández^{5,6}, David Lafrenière², Izan de Castro Leão¹⁴, Christophe Lovis¹, Lison Malo^{2,8}, Claudio Melo¹⁹, Lucile Mignon^{1,12}, Christoph Mordasini²⁰, Francesco Pepe¹, Rafael Rebolo^{5,6,21}, Jason Rowe²², Nuno C. Santos^{9,10}, Damien Ségransan¹, Alejandro Suárez Mascareño^{5,6}, Stéphane Udry¹, Diana Valencia¹³, Gregg Wade^{23,24}, José L. A. Aguiar¹⁴, Khaled Al Moulla^{9,1}, Babatunde Akinsanmi¹, Nicholas W. Borsato^{25,26}, Charles Cadieux², Yann Carteret¹, Ana Rita Costa Silva^{9,10,1}, Eduardo A. S. Cristo⁹, Thierry Forveille¹², Yolanda G. C. Frensch^{1,27}, Nicole Gromek¹⁵, Monika Lendl¹, Bibiana Prinoth²⁶, Angelica Psaridi^{1,29,30}, Atanas K. Stefanov^{5,6}, Brian Thorsbro^{28,7}, Drew Weissman¹⁵

(Affiliations can be found after the references)

Received July 4th 2025; Accepted August 26th 2025

ABSTRACT

Ultra-hot gas giants like WASP-121b provide unique laboratories for exploring atmospheric chemistry and dynamics under extreme irradiation conditions. Uncovering their chemical composition and atmospheric circulation is critical for tracing planet formation pathways. Here, we present a comprehensive atmospheric characterization of WASP-121b using high-resolution transit spectroscopy across the optical to infrared with HARPS, NIRPS, and CRIRES+, spanning nine transit events. These observations are complemented with five TESS photometric sectors, two EulerCam light curves simultaneous to the HARPS and NIRPS transits, and an extensive radial velocity dataset to refine WASP-121b's orbital parameters. A cross-correlation analysis detects iron (Fe), carbon monoxide (CO) and vanadium (V) absorption signals with SNR of 5.8, 5.0, 4.7, respectively. Our retrieval analysis constrains the water (H₂O) abundance to $-6.52^{+0.49}_{-0.68}$ dex, although its absorption signal is effectively muted by the hydride (H⁻) continuum. We constrain the relative abundances of volatile and refractory elements – crucial diagnostic of atmospheric chemistry, evolution, and planet formation pathways. The retrieved abundance ratios are broadly consistent with expected values of a solar composition atmosphere in chemical equilibrium, likely indicating minimal disequilibrium chemistry alterations at the probed pressures ($\sim 10^{-4} - 10^{-3}$ bar). We update the orbital parameters of WASP-121b with its largest radial velocity dataset to date. By comparing orbital velocities derived from both the radial velocity analysis and the atmospheric retrieval, we determine a non-zero velocity offset caused by atmospheric circulation, $\Delta K_p = -15 \pm 3 \text{ km s}^{-1}$ (assuming $M_* = 1.38 \pm 0.02 M_\odot$), consistent with predictions from either drag-free or weak-drag 3D global circulation models, while cautioning the non-negligible dependence on the stellar mass assumed. These results place new constraints on the thermal structure, dynamics, and chemical inventory of WASP-121b, highlighting the power of multi-wavelength, high-resolution spectroscopy to probe exoplanetary atmospheres.

Key words. instrumentation: spectrographs – methods: observational – techniques: spectroscopic – planets and satellites: atmospheres – planets and satellites: composition – planets and satellites: gaseous planets

1. Introduction

Ultra-hot Jupiters represent the hottest class of gas giant exoplanets ($T_{\text{eq}} > 2000 \text{ K}$), showcasing extreme atmospheric conditions driven by the proximity to their hot, early type (typically A or F) host star (e.g. Hellier et al. 2009; Collier Cameron et al. 2010; West et al. 2016; Delrez et al. 2016; Gaudi et al. 2017; Lund et al. 2017; Anderson et al. 2018). These planets receive an enormous stellar irradiation, orders of magnitude larger than observed in Solar-system planets, driving the thermal dissociation of molecules and the ionisation of atoms (Kitzmann et al. 2018; Parmentier et al. 2018; Hoeijmakers et al. 2018, 2019), atmospheric circulations (Arcangeli et al. 2019; Seidel et al. 2019,

2020a, 2021; Seidel et al. 2025), heat transport through dissociation/recombination of molecular hydrogen (H₂; Bell & Cowan 2018; Tan & Komacek 2019), and condensation of metals on the nightside (Ehrenreich et al. 2020; Gandhi et al. 2023; Pelletier et al. 2023). At such elevated temperatures, not only do new spectral features appear, but lines already present at lower temperatures also have their amplitude and width bolstered. This overall increase in the line strength relative to the continuum makes ultra-hot gas giants ideal targets for atmospheric characterization via transmission and emission spectroscopy.

High-resolution transmission and emission spectroscopy have proven valuable methods to characterise the atmosphere of such hot planets, in tandem with the cross-correlation technique (e.g. Snellen et al. 2010; Brogi et al. 2012; Birkby et al.

* Corresponding author: valentina.vaulato@unige.ch

2013; Hoeijmakers et al. 2018, 2019, 2020a; Ehrenreich et al. 2020; Prinoth et al. 2022, 2023; Prinoth et al. 2025; Vaulato et al. 2025). The cross-correlation method has been broadly used to infer the chemical composition of planetary atmospheres, as well as their dynamics (Seidel et al. 2020b; Seidel et al. 2025; Wardenier et al. 2024; Ramkumar et al. 2025), by resolving individual spectral lines of broad molecular bands and measuring the planet’s Doppler shift at the level of km s^{-1} precisions. Unlike low-resolution spectroscopy, high-resolution data are typically self-calibrated by removing broadband flux variations and temporal changes in flux at each wavelength, thus lacking reliable information on the planet’s continuum, see however Santos et al. (2020). Cross-correlation is then limited in the sense of being insensitive to residual broadband variations. Brogi & Line (2019) introduced a statistically robust atmospheric retrieval framework to overcome such limitations and access the chemical composition and temperature-pressure profile of planetary atmospheres.

Discovered by Delrez et al. (2016), WASP-121b is a benchmark ultra-hot Jupiter target ($R_p = 1.753 \pm 0.036 R_J$, $M_p = 1.157 \pm 0.070 M_J$, $P_{\text{orb}} \sim 1.27$ days, $T = 2358 \pm 52$ K; Delrez et al. 2016; Bourrier et al. 2020; Patel & Espinoza 2022) in an highly misaligned orbit ($\lambda = 87.20^{+0.41}_{-0.45}$ deg, Bourrier et al. 2020) around its F6V-type star. It has been extensively observed in both emission and transmission across a broad range of wavelengths in low and high-resolution (e.g. Evans et al. 2016; Hoeijmakers et al. 2020b; Sing et al. 2024; Seidel et al. 2025; Gapp et al. 2025).

Exospheric species such as excited hydrogen (H_α), and ionised iron (Fe II) and calcium (Ca II) (firstly detected at high altitudes by Sing et al. 2019; Borsa et al. 2021) are found to extend beyond the Roche limit that implies the planet experiences mass loss. The 4-UT VLT/ESPRESSO (Pepe et al. 2021) partial transit data obtained during the commissioning of the spectrograph (Borsa et al. 2021) were also used in Seidel et al. (2023) to interpret the blue-shifted sodium feature (firstly identified by Hoeijmakers et al. 2020b) as a signature of equatorial day-to-nightside winds crossing the evening limb. In particular, Seidel et al. (2023) characterized the secondary Na feature visible only in egress, far more offset. Maguire et al. (2023) constrained the relative abundances of metals by stacking high-resolution optical spectra obtained with ESPRESSO (two transits in 1-UT mode and an archival partial transit in 4-UT mode from commissioning data, the same data as used by Borsa et al. (2021) and Seidel et al. (2023)), retrieving abundance ratios generally consistent with stellar values, albeit with some exceptions. Further insights into atmospheric dynamics were gained through phase-resolved infrared transmission spectra from Gemini-S/IGRINS (Park et al. 2014). Carbon monoxide and H_2O were detected and interpreted with 3D global circulation models (GCM; Wardenier et al. 2024) suggesting the importance of atmospheric drag. A new 4-UT ESPRESSO dataset, completing the partial transit reported in Borsa et al. (2021), Seidel et al. (2023), and Maguire et al. (2023), allowed Seidel et al. (2025) to unveil an onion-layered upper atmosphere. In this configuration (see their Figure 3), atomic iron (Fe I) traces sub-to-antistellar flows (day-to-night winds) at \sim millibar pressures; sodium (Na I) probes jet streams from the morning to evening terminator at lower pressures ($\sim 10^{-5}$ bar), and the hydrogen ions (H I) track the remarkably red- to blue-shifted signature of the jet at very high altitudes ($\sim 10^{-6}$ bar).

In the context of atmospheric characterisation, Hoeijmakers et al. (2024) reported on significant detections (earlier reported by Hoeijmakers et al. 2020b) of atomic calcium (Ca I), vanadium (V I), chromium (Cr I), manganese (Mn I), iron

(Fe I), cobalt (Co I), and nickel (Ni I) in ESPRESSO day-side spectra, while atomic titanium (Ti I) and titanium oxide (TiO) were notably not detected in cross-correlation. These authors surmised that Ti-bearing species condense on the nightside and remain cold-trapped there, thus inaccessible to both transmission and emission spectroscopy. Merritt et al. (2021) used VLT/UVES (Dekker et al. 2000) transit time-series to confirm robust detections of Fe I, Cr I, V I, Ca I, K I and exospheric H I and Ca II, while adding a novel detection of ionised scandium (Sc II). However, Prinoth et al. (2025), leveraging the high signal-to-noise ratio of 4-UT ESPRESSO transit observations, successfully detected titanium (Ti), albeit finding the signal to be notably weaker than expected. Meanwhile, titanium oxide (TiO) still remains undetected, likely due to limitations in the current line lists. Additionally, Prinoth et al. (2025) reported a plethora of detected species (i.e. neutral atoms like H I, Li I, Na I, Mg I, K I, Ca I, Ti I, Cr I, Mn I, Fe I, as well as excited atoms such as V II, Fe II, Co I, Ni I, Ba II, Sr I, and Sr II) confirming and expanding upon previous literature findings (Merritt et al. 2021; Silva et al. 2022; Hoeijmakers et al. 2024). Optical (ESPRESSO) and infrared (VLT/CRIRES+; Dorn et al. 2023) data were used by Pelletier et al. (2024) to measure the volatile-to-refractory budget and C/O ratio. An analogue study was carried out in Smith et al. (2024) using IGRINS data, retrieving overall similar properties for the dayside atmosphere of WASP-121b, but arriving to contrasting conclusions regarding the atmospheric volatile-to-refractory enrichment. Indeed, Pelletier et al. (2024) concluded that the atmosphere of WASP-121b is likely volatile-rich, while Smith et al. (2024) preferred a super-stellar refractory-to-volatile ratio, despite both finding a C/O ~ 0.70 under the assumption of chemical equilibrium conditions. On this topic, a recent work by Evans-Soma et al. (2025) reports on a super-stellar C/H, O/H and C/O ratios (along with robust water, carbon monoxide, and silicon monoxide detections) obtained with a single JWST observation, suggesting that pebbles and planetesimal are important in the formation pathway of giant planets. Among the latest published results, the Near-Infrared Planet Searcher (NIRPS; Bouchy et al. 2025) has confidently detected both H_2O and its thermal dissociation byproduct, OH, in the thermal spectrum of WASP-121b, providing evidence for water dissociation that aligns with model predictions (Bazinet et al. 2025).

In this paper, we report on the first near-infrared high resolution spectroscopic NIRPS observations of WASP-121b’s transit, combined with simultaneous HARPS and archival CRIRES+ transit time series. The scientific objective is to characterise the chemical composition and ongoing chemical processes in WASP-121b’s atmosphere. Furthermore, we complement the spectroscopic data with high-precision radial velocity measurements to refine the orbital parameters of the system.

Section 2 describes the spectroscopic and photometric observations. Section 3 presents a global fit to the RVs and photometry in order to improve the planetary parameters, and particularly the RV semi-amplitude. It includes five TESS sectors, and a total of 1261 public RV measurements from CORALIE, HARPS, ESPRESSO, and NIRPS; this is the largest RV dataset ever used to characterize WASP-121 b. Section 4 illustrates the data processing for atmospheric analyses, the cross-correlation approach, and the atmospheric retrieval recipe. Section 5 discusses the detections of cross-correlation functions, the key retrieval results, and a comparison with previous results in the context of global circulation models, and discuss their implications.

2. Observations

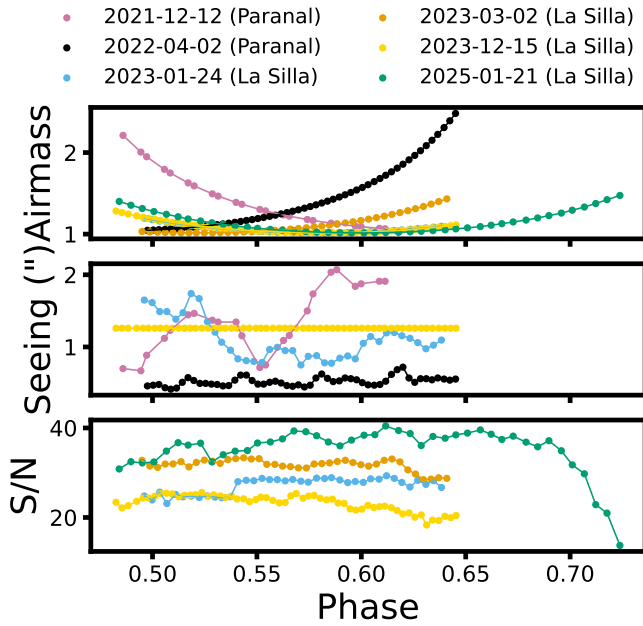


Fig. 1: Observing conditions as a function of phase. The blue, orange, yellow, and green points correspond to NIRPS (and simultaneous HARPS) observations, while the pink and black points represent CRRES+ observations in the H - and K -bands, respectively. Top panel and mid panel illustrate the airmass and the average atmospheric Dimm seeing (i.e. value for the differential image monitor) evolving during the nights, respectively. The Dimm seeing is averaged for each observations (i.e. average between the start and the end of each observation). The bottom panel shows the signal-to-noise ratio (extracted from the fits header) changing during the nights.

2.1. Spectroscopic transit observations with NIRPS and HARPS

We observed a total of four transits of WASP-121b across the disc of its relatively bright host star WASP-121 ($V=10.51$, $J=9.63$; Høg et al. 2000; Cutri et al. 2003, respectively) simultaneously with the high-resolution spectrographs HARPS (Pepe et al. 2000) and the new fiber-fed, ultra stable and high-precision Near-Infrared Planet Searcher (NIRPS; Bouchy et al. 2025). NIRPS has been designed (i) to expand the wavelength coverage from the optical to the Y , J , and H bands, (ii) to leverage avantgarde adaptive optics, and (iii) to operate simultaneously with HARPS at the 3.6-m telescope in La Silla, Chile. We observed WASP-121b transits on 2023-01-24 (Night 1) and 2023-03-02 (Night 2) as part of the commissioning (program ID 60.A-9109) of the NIRPS instrument, and on 2023-12-15 (Night 3) and 2025-01-21 (Night 4) as part of the ESO GTO program IDs 112.25P3.001 and 112.25P3.003, respectively (PI: F. Bouchy). Of those, three transit observations (i.e. Nights 2, 3, and 4) have been gathered simultaneously with HARPS in High Accuracy Mode (HAM) and NIRPS in High Efficiency (HE, Night 3 and 4) and High Accuracy (HA, Night 2) modes (Bouchy et al. 2025), whereas the first transit was observed with NIRPS only. The transit of WASP-121b has been partially observed by

HARPS and NIRPS also on 2025-02-27, but the dataset was discarded and not used in this work because of major technical issues (problems with the hydraulic system causing the dome vignetting the mirror) severely impacting the quality of the data (low signal-to-noise ratio). We refer the reader to Table 1 and Figure 1 for a summary of the observation status.

The transit duration (from the first to the fourth contact) is about 3 hours, and the total observing time (transit duration + baseline before ingress and after egress) was about 5 hours for all transits. All spectra were reduced by the automated HARPS and NIRPS Data Reduction Softwares (DRS version 3.2.5 and 3.2.0, respectively; Pepe et al. 2021), which yield the echelle-order merged (S1D) and echelle-order separated (S2D) spectra corrected for the Barycentric Earth Radial Velocity (BERV). The starting point of the atmospheric analysis are the HARPS and NIRPS S2D_BLAZE_A.fits files, namely the science fiber acquired and neither blaze nor telluric corrected spectra. We thus work on a temporal series of spectra $f(\lambda, t) = f(\lambda, t)|_{\text{BERV}}$ (i.e. provided in the barycentric rest frame).

2.2. Spectroscopic transit observations with CRRES+

We supplement our optical and near-infrared observations with two CRRES+ transit time-series (Night 5 on 2021-12-12, PI: Romain Allart, program ID: 108.22CZ; Night 6 on 2022-04-02, PI: Brian Thorsbro, program ID 109.23D2). CRRES+ is a high-resolution infrared slit spectrograph (Follert et al. 2014; Dorn et al. 2023) installed at UT3 of the Very Large Telescope in Paranal, Chile. The observations are gathered in the K (Night 5) and H (Night 6) spectroscopic bands, respectively. In the K -band, the exposures were taken in the ABBA nodding sequence (alternated position on the slit) to best subtract contributions from sky background sources, while in the H -band they were gathered in an unconventional AAABBBBBBAAA nodding to reduce time spent on nodding. To preserve a better time sampling and avoid additional blurring of the rapidly accelerating planetary signal, we choose not to perform our analysis on the combined AB spectra, but instead we analyse the A and B output spectra individually. Specifically, we treat the A nodding positions and the B nodding positions as separate time series for both the H and K -band observations. That said, neither H nor K -band data are background subtracted, but this is not worrying as it will be cared of by the principal component analysis at a later stage of the data reduction pipeline (see Section 4 for details).

2.3. Simultaneous photometry with EulerCam

Simultaneously with the NIRPS+HARPS observations on Nights 3 and 4, we acquired two photometric transits using the EulerCam instrument mounted on the ESO 1.2-meter Swiss Euler telescope (Lendl et al. 2012) on UT nights 2023-12-15 and 2025-01-21. The goal of our observations was to refine the ephemerides and to identify and mitigate the impact of any starspot occultations. The observations were taken in Geneva- r and Geneva- v filters with an exposure time of 30 and 45 seconds. The image reduction includes bias, flat and over-scan correction, and the aperture photometry uses the prose framework (Garcia et al. 2022). The optimal differential photometry is performed following Broeg et al. (2005). The transit light curves are modelled using the CONAN package (Lendl et al. 2017). The best-fit transit model along with the detrended light curves is shown in Figure 2. The obtained ephemerides are compatible with Bour-

Table 1: Log of NIRPS, HARPS and CRIRES+ transit observations.

Date	Night 5 2021-12-12	Night 6 2022-04-02
CRIRES+	<i>K</i> -band	<i>H</i> -band
Resolving power	86 000 - 92 000	86 000 - 92 000
Number of spectra	23	54
Avg. seeing ["]	1.36	0.52
Avg. S/N	-	-

Date	Night 1 2023-01-24	Night 2 2023-03-02	Night 3 2023-12-15	Night 4 2025-01-21
NIRPS	Comm. 8	Comm. 9	GTO	GTO
Resolving power	80 000	80 000	80 000	80 000
Observing mode	HE	HA	HE	HE
Number of spectra	39	40	58	44
Exp. time [s]	400	400	300	600
Number of exp.	39	40	58	44
Avg. seeing ["]	1.1	0.9	0.8	0.5
Avg. S/N order 57 *	41	45	36	54
S/N <i>Y</i> band	32	38	28	40
HARPS	Comm. 8	Comm. 9	GTO	GTO
Resolving power	120 000	120 000	120 000	120 000
Observing mode	-	HAM	HAM	HAM
Number of spectra	-	26	54	82
Exp. time [s]	-	600	300	300
Number of exp.	-	26	54	82
S/N at 550 nm	-	30	N.A.	18

Notes: *In NIRPS spectra, we choose as reference the spectral order 57 centred at 16,285 Å (*H* band) because it is little affected by telluric absorption lines. Night 1 and 2 belong to commissioning runs 8 and 9 (pre-GTO time), respectively.

rier et al. (2020). Thus, we choose to use the timings derived from Bourrier et al. (2020). Furthermore, we used PyTranSpot (Juvan et al. 2018; Chakraborty et al. 2024) to search for any starspot occultations by simultaneously fitting a transit and spot model. In conclusion, we found no evidence of starspot contamination in the transit light curves.

3. Refined system parameters

In order to refine the orbital solution of WASP-121b, in particular the radial velocity (RV) semi-amplitudes used to calculate the value and uncertainty of ΔK_p (see Sect. 5.3), we carry out a simultaneous fit of all available RV datasets and all TESS photometric data with the *juliet*¹ software (Espinoza et al. 2019). *juliet* uses the *radvel* package (Fulton et al. 2018) and the *batman* package (Kreidberg 2015) to model RVs and transits respectively, exploring the parameter space via importance nested sampling with the *dynesty* package (Speagle 2020). It employs random walk sampling with 500 live points by default. Gaussian processes (GPs) can be incorporated via the *celerite* package (Foreman-Mackey et al. 2017).

The fit incorporates ten RV datasets and five TESS sectors, which are described in Tables 2 and 3, respectively. We remove all in-transit RVs affected by the Rossiter-McLaughlin effect, but retain the out-of transit baseline-establishing observations

for these datasets, which notably allows us to incorporate three such sets of ESPRESSO data. For the TESS photometry, we use the Presearch Data Conditioning Simple Aperture Photometry (PDC-SAP) light curves (Stumpe et al. 2012, 2014; Smith et al. 2012) generated by the TESS Science Processing Operations Center (SPOC, Jenkins et al. 2016) at NASA Ames Research Center. We obtain the light curves from the Mikulski Archive for Space Telescopes (MAST) archive. The RV data, meanwhile, are obtained from the Data & Analysis Center for Exoplanets (DACE) platform². The specific data reduction system (DRS) versions used for each dataset, and the median RV errors, are listed in Table 2. We treat datasets from different modes (e.g. NIRPS in high accuracy or high efficiency mode), and/or from before and after instrument upgrades (e.g. the ESPRESSO fibre link replacement, Pepe et al. 2021), as separate instruments for the purposes of this analysis. This allows us to account for any offsets between the datasets.

We pre-detrend the TESS sectors using a GP with the (approximate) Matern 3/2 kernel, as implemented in *celerite*, via a two-step process where we employ the out-of transit data to constrain the GP which we then apply to the in-transit data. We first mask the in-transit data in each sector, with a 5h padding of the transit window. Next, we fit a GP to the out-of-transit data in each sector, with broad log-uniform priors of $\mathcal{J}(1 \times 10^{-6}, 1 \times 10^6)$ for $\sigma_{\text{GP,sector}}$ and $\mathcal{J}(1 \times 10^{-3}, 1 \times 10^3)$ for $\rho_{\text{GP,sector}}$. We also fit

¹ Available at <https://github.com/nespinoza/juliet>

² Available online at <https://dace.unige.ch>

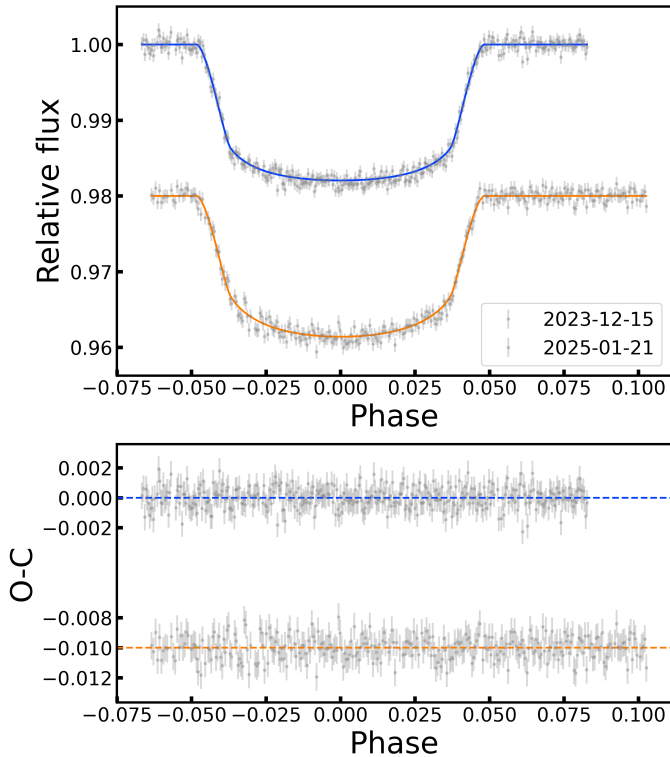


Fig. 2: Simultaneous photometry with EulerCam. *Top*: Detrended EulerCam light curves with the best-fit transit models overlaid on top. *Bottom*: The residuals for each observation. The horizontal dashed lines indicate the continuum at zero.

the flux offset $m_{\text{flux,sector}}$, and jitter $\sigma_{w,\text{sector}}$ for each sector using the out-of-transit data, setting the dilution factor $m_{\text{dilution,sector}}$ to 1 for all sectors. We then fix the resulting parameters for the final fit, in which we use only the in-transit data.

We fit the following parameters in the global fit: stellar density ρ ; the period P_b , RV semi-amplitude K_b (i.e. the stellar reflex motion), time of transit $t_{0,b}$, planet-to-star radius ratio p_b , and impact parameter b_b for WASP-121b; the systemic radial velocity $\mu_{\text{instrument}}$ and jitter $\sigma_{w,\text{instrument}}$ for each RV instrument; and common limb-darkening parameters $q_{1,\text{TESS}}$ and $q_{2,\text{TESS}}$ for all TESS sectors. For the limb-darkening parameters, we used the quadratic law parametrisation of Kipping (2013), with uninformative priors of $\mathcal{U}(0, 1)$. Given the very short period of the planet, we fix the eccentricity to 0. For P_b , $t_{0,b}$, p_b , and b_b we use the values of Bourrier et al. (2020) as the central point of normal priors. As we are especially interested in K_b , we take a broad prior of $\mathcal{U}(0, 1000) \text{ m s}^{-1}$. For the systemic radial velocities we set uniform priors between the minimum and maximum RV values for each instrument; for the RV jitter, we set log-uniform priors of $\mathcal{J}(0.001, 100) \text{ m s}^{-1}$. The host star is an active fast rotator, and this activity has previously been reported to affect the RVs, necessitating their detrending (Delrez et al. 2016; Bourrier et al. 2020). For this analysis, we also simultaneously fit a separate GP with the (approximate) Matern 3/2 kernel to each dataset except for the single-night ESPRESSO1, ESPRESSO2, and ESPRESSO5 datasets. These three datasets were excluded because their very short baselines do not allow for a good characterization of the stellar activity; we also note that preliminary test fits including a GP component for these datasets showed no improvement in their RV dispersion. To constrain the GP parameters, we first fit a GP to the FWHM activity indicator time

series for each dataset, which show significant scatter and structure, similarly to Hobson et al. (2024). We take broad uniform priors of $\mathcal{U}(1, 5000)$ for σ_{GP} and $\mathcal{U}(0.1, 10)$ for ρ_{GP} . We then use the posteriors of these fits as normal priors for the RV GPs in the full fit.

The full priors and posteriors are reported in Table 4. We show the RV time series and best-fit model in Figure 3, the phase-folded RVs and model in Fig. 4 and the phase-folded TESS photometry in Fig. 5. We use the fitted stellar RV semi-amplitude $K_b = 167.97^{+5.78}_{-6.98} \text{ m s}^{-1}$ to obtain a planet RV semi-amplitude of $K_p = 218.42 \pm 1.06 \text{ km s}^{-1}$. To compute WASP-121b’s orbital velocity semi-amplitude, we use Equation 1 in Torres et al. (2010), which does not depend on the planet mass. The planet mass is measured from the juliet RV fit, thus we prefer not to assume its value a priori to derive the orbital K_p . To calculate the orbital planetary velocity, we assume a stellar mass $M_\star = 1.38 \pm 0.02 M_\odot$ (Borsa et al. 2021), an orbital inclination $i = 88.49 \pm 0.16^\circ$ (Bourrier et al. 2020), and a fixed zero eccentricity. However, K_p is directly proportional to the stellar mass which is not easy to extract in the case of F-type stars such as WASP-121 owing to the high stellar activity and fast rotation (see Section 5.3 for an in depth discussion). In this work, we assume the stellar mass extracted by Borsa et al. (2021) (see their Table 2, and Section 3 and 4), as they relied on the complete 1-UT transit dataset gathered with VLT/ESPRESSO.

The uncertainty on K_p is calculated using error propagation. In this case, K_p depends on the stellar mass, the orbital inclination, the stellar reflex velocity, and the orbital period. To compute the uncertainty on K_p , we use the finite difference method to approximate the partial derivatives. Thus, when including all available RV datasets (Table 2, Figure 4), we improve the uncertainty on both the stellar reflex motion K_b and the computed semi-amplitude orbital velocity of WASP-121b with respect to Bourrier et al. (2020) (see their Table 1).

4. Data processing for atmospheric analyses

We carry out cross-correlation and atmospheric retrieval analyses on the combined HARPS, NIRPS and CRILES+ transit time-series. In order to isolate the planetary signal, the data must first be detrended in order to remove telluric and stellar contributions that dominate the observed spectra. This involves the steps described in Pelletier et al. (2021, 2023), and recapitulated as follow: We apply a σ -clipping to the flux variation and all outliers at more than 6σ are flagged and removed. We also discard those bad exposures affected by residual systematics. Heavily telluric contaminated regions are masked out (e.g., 0.6868–0.694 μm , 1.345–1.4465 μm , 1.7995–1.96 μm). Near-infrared to infrared spectra are notoriously polluted by Earth’s atmospheric emission (i.e. OH) and absorption lines (i.e. H₂O, CH₄, CO₂, O₂). An additional mask-clipping is applied to data below 0.5 (considering the spectrum as normalised to one) to mask deep telluric spectral lines outside those highly telluric contaminated regions already discarded. All spectra are adjusted to the same continuum level according to a double filtering approach (Gibson et al. 2020): a first box-filter of width 51 pixels is applied to each exposure, smoothed by a Gaussian convolution with a standard deviation of 100 pixels applied to each individual order. This accounts for continuum variations or blaze variations along the observed time-series.

A second order polynomial is used to fit the built out-of-transit median spectrum for one night (done night by night) and then divided from each single exposure to remove first-order

Table 2: RV datasets for the *juliet* modelling.

Instrument	RVs	Time span	Mode/version	Program ID	DRS version	Median RV error [m s ⁻¹]
CORALIE1	31	11/09/2013 - 08/10/2014	CORALIE07	730	3.4	19.3
CORALIE2	19	18/11/2014 - 10/03/2015	CORALIE14	730	3.8	41.6
HARPS	399	01/01/2018 - 03/02/2024	-	0100.C-0750, 112.25P3, 60.A-9109	3.5	22.8
ESPRESSO2	10	01/12/2018	HR21, pre-upgrade	1102.C-0744	3.3.1	2.9
ESPRESSO1	28	07/01/2019	MR42, pre-upgrade	60.A-9128	3.3.1	5.8
ESPRESSO3	103	27/01/2021 - 05/03/2021	HR11, post-upgrade	106.21R1, 106.21R1	3.3.1	10.4
ESPRESSO4	298	12/01/2021 - 17/04/2021	HR21, post-upgrade	105.20BN, 106.21QM	3.3.1	5.2
ESPRESSO5	10	24/09/2023	MR42, post-upgrade	111.24J8	3.3.1	31.3
NIRPS2	302	25/01/2023 - 03/02/2024	HE	112.25P3, 60.A-9109	3.2.0	52.7
NIRPS1	61	03/03/2023 - 06/03/2023	HA	60.A-9109	3.2.0	46.2

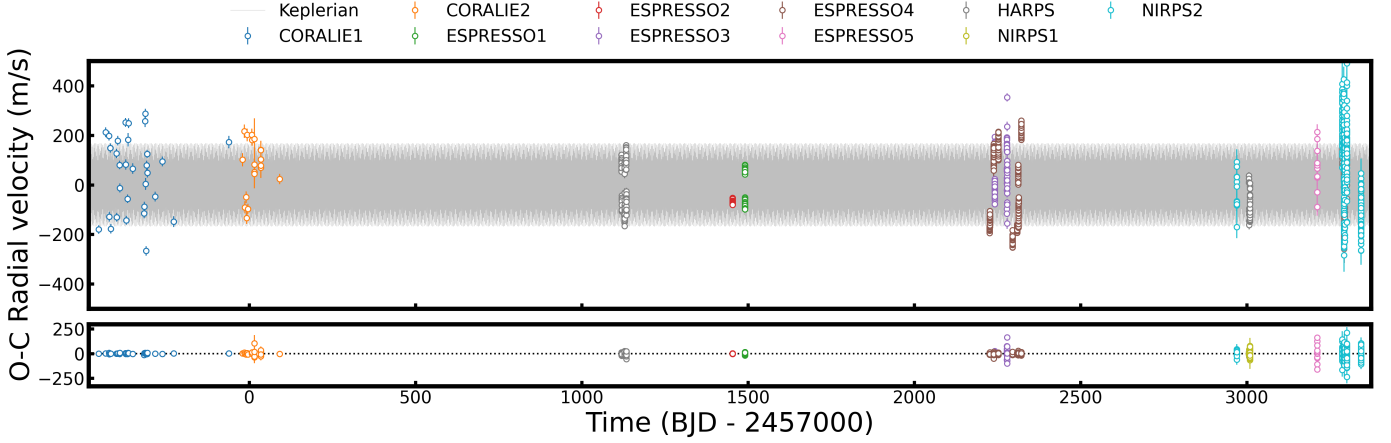


Fig. 3: Top panel: RV time series (coloured dots) and best-fit Keplerian model (grey line) for the *juliet* fit of the WASP-121 public RVs. The fitted instrumental offsets $\mu_{\text{instrument}}$ have been subtracted from each time series. Bottom panel: residuals of the fit.

Table 3: TESS datasets for the *juliet* modelling.

TESS sector	Camera	CCD	Time span
7	3	2	08/01/2019 - 01/02/2019
33	3	1	18/12/2020 - 13/01/2021
34	3	2	14/01/2021 - 08/02/2021
61	3	2	18/01/2023 - 12/02/2023
87	3	1	18/12/2024 - 14/01/2025

stellar or telluric residual lines. The Principal Component Analysis (PCA) routine is employed to remove any telluric lines and stellar residuals in the data and reconstruct the observed spectral temporal series. After testing, we decide to remove 5 principal components to best compromise on the cleanliness of the data while preserving the planetary signal. Finally, all column pixels having a standard deviation greater than 5σ that of the spectral order are masked out. Results of the detrending steps for NIRPS, HARPS, and CRIRES+ transit time-series are shown in Figure A.1 in Appendix A.

4.1. Cross-correlation analysis

As described by Vaulato et al. (2025), we use SCARLET (Benneke & Seager 2012, 2013; Benneke 2015; Benneke et al. 2019; Pelletier et al. 2021) to generate synthetic transmission spectra of WASP-121b. SCARLET models use (i) H₂-H₂ and H₂-He collision-induced opacities (Borysow 2002), (ii) molec-

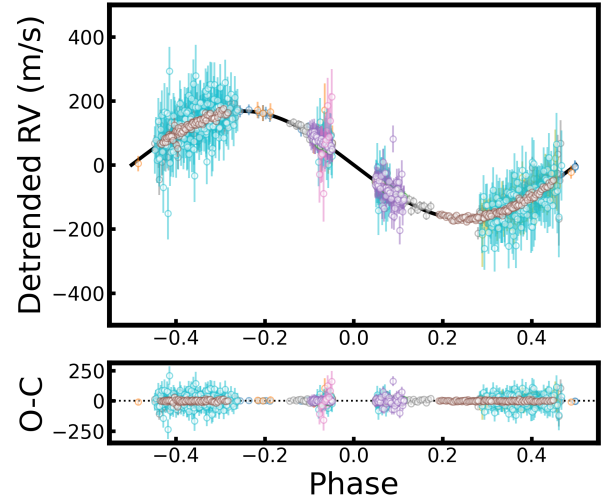


Fig. 4: Top panel: phase-folded RVs (coloured dots) and best-fit Keplerian model (black line). The colours of the RV points match those in Fig. 3. Both the fitted instrumental offsets and the GP components (where applicable) have been subtracted from each time-series. Bottom panel: residuals of the fit.

ular cross-sections for H₂O (Polyansky et al. 2018), OH (Rothman et al. 2010), CO (Rothman et al. 2010; Li et al. 2015), and TiO (McKemmish et al. 2019), (iii) atomic cross-sections for Fe, Ti, V, Mn, Mg, Ca, Cr, Ni, Na, Y, Ba, Sc, C from

Table 4: Prior and posterior planetary parameter distributions obtained with juliet for WASP-121.

Parameter	Prior	Posterior
μ_{CORALIE1} [m s ⁻¹]	$\mathcal{U}(18928.81, 76823.52)$	$38124.08^{+16.63}_{-17.27}$
$\sigma_{\text{w,CORALIE1}}$ [m s ⁻¹]	$\mathcal{J}(0.001, 100)$	$0.45^{+7.47}_{-0.44}$
μ_{CORALIE2} [m s ⁻¹]	$\mathcal{U}(19047.03, 77104.58)$	$38336.67^{+18.54}_{-19.88}$
$\sigma_{\text{w,CORALIE2}}$ [m s ⁻¹]	$\mathcal{J}(0.001, 100)$	$0.63^{+7.78}_{-0.60}$
$\mu_{\text{ESPRESSO1}}$ [m s ⁻¹]	$\mathcal{U}(19032.28, 76495.73)$	$38167.08^{+3.44}_{-2.66}$
$\sigma_{\text{w,ESPRESSO1}}$ [m s ⁻¹]	$\mathcal{J}(0.001, 100)$	$8.73^{+3.80}_{-3.33}$
$\mu_{\text{ESPRESSO2}}$ [m s ⁻¹]	$\mathcal{U}(19041.41, 76296.34)$	$38180.49^{+2.90}_{-3.25}$
$\sigma_{\text{w,ESPRESSO2}}$ [m s ⁻¹]	$\mathcal{J}(0.001, 100)$	$2.77^{+1.85}_{-1.06}$
$\mu_{\text{ESPRESSO3}}$ [m s ⁻¹]	$\mathcal{U}(18944.17, 76794.85)$	$38250.81^{+1889.35}_{-1812.77}$
$\sigma_{\text{w,ESPRESSO3}}$ [m s ⁻¹]	$\mathcal{J}(0.001, 100)$	$38.27^{+4.30}_{-4.08}$
$\mu_{\text{ESPRESSO4}}$ [m s ⁻¹]	$\mathcal{U}(18938.14, 76776.31)$	$38130.07^{+38.19}_{-32.04}$
$\sigma_{\text{w,ESPRESSO4}}$ [m s ⁻¹]	$\mathcal{J}(0.001, 100)$	$0.34^{+0.89}_{-0.29}$
$\mu_{\text{ESPRESSO5}}$ [m s ⁻¹]	$\mathcal{U}(10219.46, 41957.50)$	$20526.92^{+21.14}_{-21.74}$
$\sigma_{\text{w,ESPRESSO5}}$ [m s ⁻¹]	$\mathcal{J}(0.001, 100)$	$79.73^{+11.85}_{-11.82}$
μ_{HARPS} [m s ⁻¹]	$\mathcal{U}(19041.74, 77090.00)$	$38342.13^{+21.53}_{-16.40}$
$\sigma_{\text{w,HARPS}}$ [m s ⁻¹]	$\mathcal{J}(0.001, 100)$	$0.013^{+0.091}_{-0.010}$
μ_{NIRPS1} [m s ⁻¹]	$\mathcal{U}(19122.74, 77361.06)$	$35802.25^{+2208.72}_{-2399.00}$
$\sigma_{\text{w,NIRPS1}}$ [m s ⁻¹]	$\mathcal{J}(0.001, 100)$	$0.37^{+8.85}_{-0.37}$
μ_{NIRPS2} [m s ⁻¹]	$\mathcal{U}(19053.58, 77764.47)$	$38366.56^{+1148.79}_{-1089.14}$
$\sigma_{\text{w,NIRPS2}}$ [m s ⁻¹]	$\mathcal{J}(0.001, 100)$	$48.09^{+6.44}_{-5.72}$
P_b [d]	$\mathcal{N}(1.27492504, 0.001)$	$1.274924803^{+0.000000039}_{-0.000000040}$
$t_{0,p1}$ [BJD]	$\mathcal{N}(2458119.72074, 0.01)$	$2458119.720725^{+0.0000048}_{-0.000047}$
K_b [m s ⁻¹]	$\mathcal{U}(0, 1000)$	$167.97^{+5.78}_{-6.98}$
ρ [kg m ⁻³]	$\mathcal{J}(100, 10000)$	$642.64^{+4.47}_{-4.91}$
P_b	$\mathcal{N}(0.12355, 0.1)$	$0.12142^{+0.00014}_{-0.00015}$
b_b	$\mathcal{N}(0.1, 0.1)$	$0.085^{+0.032}_{-0.038}$
$q_{1,\text{TESS}}$	$\mathcal{U}(0, 1)$	$0.223^{+0.017}_{-0.017}$
$q_{2,\text{TESS}}$	$\mathcal{U}(0, 1)$	$0.230^{+0.024}_{-0.023}$
$\sigma_{\text{GP,CORALIE1}}$	$\mathcal{N}(428.64, 82.00)$	$94.53^{+17.64}_{-15.32}$
$\rho_{\text{GP,CORALIE1}}$	$\mathcal{N}(1.60, 0.45)$	$1.33^{+0.29}_{-0.30}$
$\sigma_{\text{GP,CORALIE2}}$	$\mathcal{N}(238.04, 93.20)$	$70.84^{+24.46}_{-18.93}$
$\rho_{\text{GP,CORALIE2}}$	$\mathcal{N}(0.86, 1.29)$	$0.84^{+0.53}_{-0.46}$
$\sigma_{\text{GP,ESPRESSO3}}$	$\mathcal{N}(4935.53, 96.44)$	$4870.80^{+81.67}_{-84.61}$
$\rho_{\text{GP,ESPRESSO3}}$	$\mathcal{N}(0.1008, 0.0014)$	$0.10201^{+0.00103}_{-0.00069}$
$\sigma_{\text{GP,ESPRESSO4}}$	$\mathcal{N}(831.27, 328.02)$	$102.91^{+43.93}_{-33.07}$
$\rho_{\text{GP,ESPRESSO4}}$	$\mathcal{N}(1.98, 0.92)$	$1.85^{+0.69}_{-0.56}$
$\sigma_{\text{GP,HARPS}}$	$\mathcal{N}(1035.30, 367.75)$	$60.06^{+33.23}_{-22.29}$
$\rho_{\text{GP,HARPS}}$	$\mathcal{N}(6.38, 2.07)$	$2.23^{+2.47}_{-1.09}$
$\sigma_{\text{GP,NIRPS1}}$	$\mathcal{N}(4915.61, 131.51)$	$4770.00^{+80.32}_{-104.19}$
$\rho_{\text{GP,NIRPS1}}$	$\mathcal{N}(0.1011, 0.0017)$	$0.1019^{+0.0016}_{-0.0013}$
$\sigma_{\text{GP,NIRPS2}}$	$\mathcal{N}(4987.01, 21.98)$	$4969.42^{+13.72}_{-16.99}$
$\rho_{\text{GP,NIRPS2}}$	$\mathcal{N}(0.10017, 0.00029)$	$0.10022^{+0.00025}_{-0.00024}$
e_b	fixed	0
ω_b [°]	fixed	90
a_b [au]	—	0.0255 ± 0.0005
i_b [°]	—	88.7 ± 0.58
$T_{14,b}$ [h]	—	2.94 ± 0.09
M_b [M _J]	—	1.1 ± 0.06
R_b [R _J]	—	1.72 ± 0.04
ρ_b [g cm ⁻³]	—	0.27 ± 0.02
$T_{\text{eq},b}$ [K]	—	2333.0 ± 59.0
S_b [S _c]	—	897.1 ± 38.0

Notes: Top: Fitted parameters. Bottom: derived orbital parameters and physical parameters.

the VALD database (Ryabchikova et al. 2015), and (iv) continuum cross-sections for H⁻ (both bound-free and free-free regimes) from Gray (2021). Molecular and atomic cross-sections are computed using HELIOS-K (Grimm & Heng 2015; Grimm et al. 2021) and chemical equilibrium abundances using FastChem (Stock et al. 2018, 2022). For our SCARLET models (Figure 6), we set up a uniform and isothermal temperature structure, and a cloud-free atmosphere, which is a reasonable assumption considering the high temperatures of ultra-hot gas giant atmospheres, particularly on daysides expected to be cloud-free (Sing et al. 2016; Helling et al. 2021).

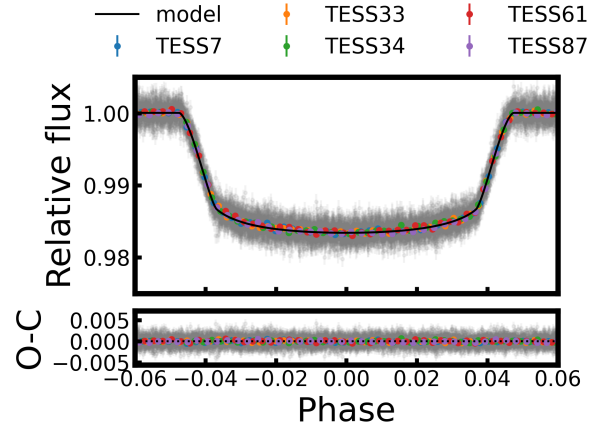


Fig. 5: Top panel: stacked phase-folded TESS photometry (grey dots), binned data for each sector (coloured dots), and best-fit model (black line) for the juliet fit of the WASP-121 TESS photometry. Bottom panel: residuals of the fit.

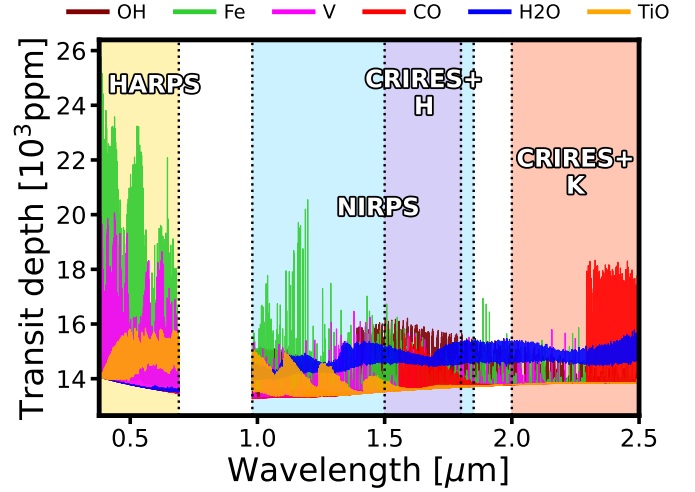


Fig. 6: Atmospheric models (transit depth as function of wavelength) for OH (brown), Fe (green), V (magenta), CO (red), H₂O (blue), and TiO (orange) generated with the SCARLET code. The shaded regions highlight the spectral coverage of each instrument: the range of wavelength of HARPS is in yellow, NIRPS region in cyan, CRIRES+ H-band and K-band in purple and orange, respectively.

The fiducial atmospheric model, initially at resolution $R = 250\,000$, is convolved with a rotational kernel (accounting for the planet's synchronous rotation), coupled with a Gaussian one-dimensional kernel to match the instrumental resolution ($R \sim 80\,000$ for NIRPS, $R \sim 120\,000$ for HARPS, and $R \sim 86\,000 - 92\,000$ for CRIRES+ for the used slit width = 0.2"). For the cross-correlation step, we generate WASP-121b's transmission model spectrum assuming a $1 \times$ solar metallicity atmosphere at temperature of 3 000 K.

Once the atmospheric model has been tailored, we calculate the cross-correlation function (CCF; Snellen et al. 2010) between the template spectrum and the cleaned data by Doppler shifting the model from velocity $v = -400$ to $+400$ km s⁻¹ with

steps of 2 km s^{-1} :

$$CCF(v, t) = \sum_{i=0}^N r_i(\lambda, t) T_i(v), \quad (1)$$

where $r_i(\lambda, t)$ is the time series of N transmission spectra as function of time t and wavelength λ , namely each pixel in the transmission spectrum at a given time t , and $T_i(v)$ are the computed model spectra Doppler shifted to a velocity v . We refer the reader to Section 4.3 in [Vaulato et al. \(2025\)](#) for further details. The computed CCFs as in Equation 1 are displayed as a function of orbital phase in two-dimensional cross-correlation trail maps for each tested chemical species.

To account for stellar contamination from the Doppler shadow, which, in our case, primarily affects HARPS optical wavelengths, we apply a 10 km s^{-1} wide mask centred at approximately $+35 \text{ km s}^{-1}$ —close to the expected systemic velocity ($+38.35 \pm 0.02 \text{ km s}^{-1}$; [Delrez et al. 2016](#)) (Figure B.1). This masking removes cross-correlation values affected by the Doppler shadow in velocity space ([Casasayas-Barris et al. 2022](#)). The CCF values are then phase-folded for different orbital configurations, namely as varying the systemic velocity (V_{sys}) from -100 to $+100 \text{ km s}^{-1}$ (1 km s^{-1} step), and the orbital velocity (K_p) from 0 to $+300 \text{ km s}^{-1}$ (1 km s^{-1} step). The individual integrations are then “stacked” across the entire transit window to enhance a strong enough planet signal which can be interpreted as a time average being summed over the orbital phases. The results are velocity-velocity diagrams called $K_p - V_{\text{sys}}$ maps ([Brogi et al. 2012](#)). The maximum signal-to-noise ratio (SNR) is measured when CCFs are co-added along the Keplerian planetary trail in the velocity space. In this work, the cross-correlation analysis is run for each instrument separately.

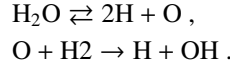
4.2. Atmospheric retrieval recipe

We perform a retrieval analysis to constrain a range of key atmospheric parameters, as summarized in Table 5. These include the volume mixing ratios (VMRs) of several atomic and molecular species—specifically, $\log_{10} \text{H}_2\text{O}$, $\log_{10} \text{CO}$, $\log_{10} \text{OH}$, $\log_{10} \text{Fe}$, $\log_{10} \text{V}$, and $\log_{10} \text{H}^-$. The VMR of a species X is defined as the logarithm (base 10) of its volume mixing ratio:

$$\log_{10} \text{VMR}_X := \log_{10} X. \quad (2)$$

In addition, we retrieve the electron density ($\log_{10} e^-$), atmospheric temperature (T), orbital velocity semi-amplitude of the planet (K_p), systemic velocity (V_{sys}), and the rotational broadening full width at half maximum (FWHM). To infer the posterior probability distributions, we use a high-resolution retrieval prescription ([Brogi & Line 2019](#); [Gibson et al. 2020, 2022](#)) which utilises SCARLET to generate the transmission spectra as detailed in [Pelletier et al. \(2021, 2023, 2024\)](#); [Bazin et al. \(2024\)](#); [Vaulato et al. \(2025\)](#). The Bayesian framework uses the likelihood approach from [Gibson et al. \(2020\)](#) and the emcee code as sampler ([Foreman-Mackey et al. 2013](#)). We run the atmospheric retrieval on the HARPS, NIRPS and CRIRES+ transits simultaneously. We also include the TESS photometric point from [Bourrier et al. \(2020\)](#) to ensure all sampled models match the true planetary radius. We opt for an atmospheric “free” retrieval approach, allowing abundances of individual species to be fitted independently as free parameters, rather than enforcing any assumptions about the atmospheric chemistry (e.g., equilibrium chemistry). The free retrieval takes input priors on the abundance profiles to be well-mixed (constant-with-altitude, hence

uniform in pressure). We assume a uniform prior distribution, $\mathcal{U}(-12, 0)$, for all absolute abundance. Assuming the high temperature of WASP-121b prevents the formation of optically-thick clouds, the continuum level is set by the H^- continuum, which is parametrised with the abundances of H^- and e^- . We set up the free retrieval to fit for abundances of H_2O and OH as representative of thermal dissociation processes, according to the following chemical reactions ([Parmentier et al. 2018](#)):



Moreover, we retrieve the abundance of CO as the main carbon-bearing species in ultra-hot Jupiters atmosphere, TiO acting as primary opacity source in optical wavelength, and the abundance of refractory species detected via cross-correlation (e.g. Fe and V). We let the retrieval free to fit for the abundance of H^- and the electron density, used to infer the continuum opacity given by H^- bound-free and free-free absorption transitions ([Arcangeli et al. 2018](#); [Parmentier et al. 2018](#); [Vaulato et al. 2025](#)).

Other than abundance parameters, the retrieval fits for the atmospheric temperature, the orbital velocities K_p and V_{sys} , and a Gaussian rotational broadening parameter to account for the observed signal appearing more “blurred” in the $K_p - V_{\text{sys}}$ space than what would be expected from the instrumental resolution alone. We assume that an isothermal profile is likely a valid approximation for the average thermal structure probed in transmission, based on [Gandhi et al. \(2023\)](#) (see their Figure 11), and [Maguire et al. \(2023\)](#) (see their Figure 3, retrieved temperature-pressure profile).

5. Results

5.1. Detections of cross-correlation functions

We detect the signatures of Fe (SNR=5.8) and V (SNR=4.7) by combining HARPS optical spectra, and CO (SNR=5.0) from CRIRES+ spectra in the K -band (Figure 7). We thus confirm previous results reported in Section 1. Neither NIRPS nor CRIRES+ H -band spectra yield a statistically significant H_2O signal (SNR ≤ 2.0) in the $K_p - V_{\text{sys}}$ space (see H_2O map in Figure 7). However, the latter datasets contribute at constraining H^- , OH, and H_2O individual abundances in the retrieval analysis, as discussed in Sect. 5.2. The non-detection of refractory elements (Fe or Ti) in the NIRPS range could be due to the fewer and weaker spectral lines exhibited by these species compared to those in the optical range of HARPS (Figure 6). However, [Vaulato et al. \(2025\)](#) showed that in the case of NIRPS observations of the ultrahot gas giant WASP-189b, these lines are damped below $\sim 1.6 \mu\text{m}$ by the H^- bound-free continuum ([Arcangeli et al. 2018](#); [Parmentier et al. 2018](#), see also Fig. 7 in [Lothringer et al. 2018](#)).

The SNR maxima of the one-dimensional cross-correlation functions of all three detected signals (top panel in Fig. 7) are slightly offset ($< 10 \text{ km s}^{-1}$, more specifically the signal peaks between $31\text{--}36 \text{ km s}^{-1}$) with respect to the reference $V_{\text{sys}} \sim 38.35 \text{ km s}^{-1}$ ([Delrez et al. 2016](#)). This could indicate the presence of winds at sub-millibar pressures (see Sect. 5.3). The consistent blueshifted signals observed for the refractory elements (e.g. Fe and V) are in agreement with sub-to-antistellar circulation in atmospheric layers, as reported by [Seidel et al. \(2025\)](#) (see their Figure 2). Alternatively, systematic offsets (different instrument by instrument) or instrumental noise might be responsible for the observed blueshifted features, hence the

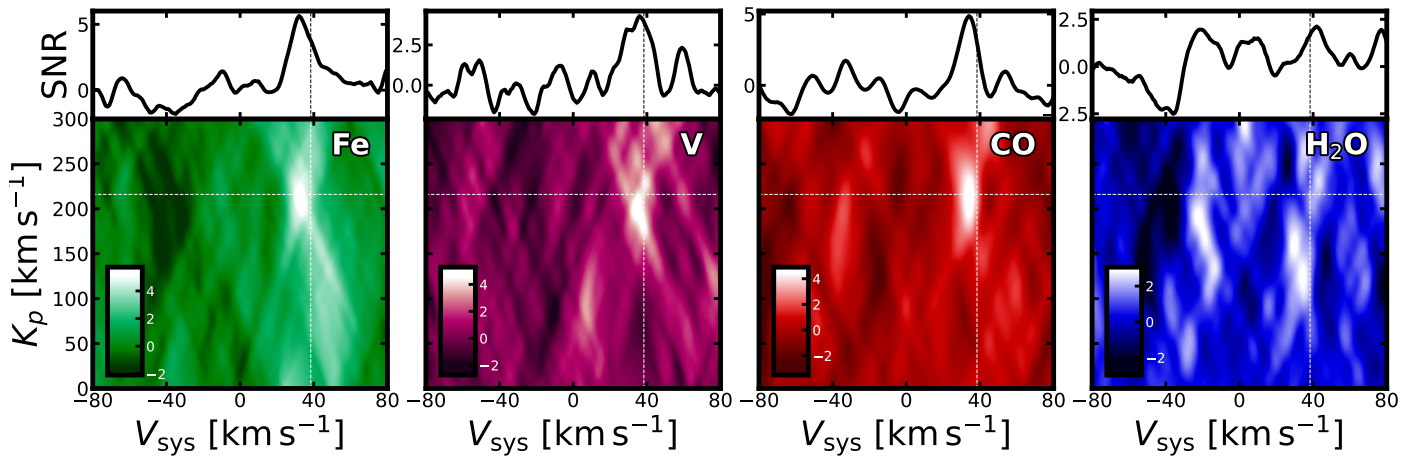


Fig. 7: Detections of CCFs for Fe (SNR=5.8), CO (SNR=5.0), and V (SNR=4.7), and non-detection of H₂O (SNR \leq 2.0) in the transmission spectrum of WASP-121b. Each squared panel shows the two-dimensional cross-correlation map in the velocity-velocity space ($K_p - V_{\text{sys}}$). The white dashed lines indicate the expected position of the planetary signal within the velocity-velocity space, namely the expected orbital ($\sim 216 \text{ km s}^{-1}$, Hoeijmakers et al. 2024) and systemic ($38.35 \pm 0.02 \text{ km s}^{-1}$, Delrez et al. 2016) velocities of WASP-121b. The rectangular panels on top depicts the one-dimensional cross-correlation of each species as signal-to-noise ratio versus systemic velocity. Detections of Fe and V are primarily driven by the optical HARPS observations, while the CO detection by the infrared CRIRES+ data (mostly K-band observations).

offset might have a non-physical meaning (not related to atmospheric circulations). However, it is worth noticing that the blueshift is fairly consistent between the HARPS-driven Fe and V detections, and the CRIRES+-driven CO detection, further supporting the hypothesis of day-to-night winds.

5.2. Retrieval results

We summarise the key results of the free atmospheric retrieval analysis on WASP-121b HARPS, NIRPS, and CRIRES+ time series combined in Figure 8, Figure 9, and Table 5. We retrieve the best-fit abundances for the chemical species injected in our model (i.e. Fe, V, CO, H₂O, OH, TiO, H⁺, and e⁻). However, retrieved absolute abundances are not informative of the underlying chemistry in a planet's atmosphere, as they significantly rely on model assumptions and, thus, are model dependent. Furthermore, retrieved absolute abundances rely on abundance constraints that are generally broad, with uncertainties of the order of 1 dex, and dependent on prior distributions (Gibson et al. 2022, see also Burningham et al. 2017). Namely, the spectra can be well-fitted by models with different parameters (e.g. reference pressure, continuum level, or planet radius). Inferring the volume mixing ratios of one specific absorbing gas of the atmosphere by directly measuring its absorption features is challenging because it depends on different combinations of the planet's radius and the mixing ratio assumed, yielding the same number density. For instance, two atmospheres with different absorber mixing ratios might have consistent pressure and densities leading to similar absorption spectral features (Benneke & Seager 2012, see their Figure 4 and Section 4.1.1). Thus, this leads to strong correlations indicating that relative abundances of species are constrained more accurately than absolute abundances (Gibson et al. 2022, see their Section 5).

To investigate the chemical composition of WASP-121b's atmosphere, we calculate abundance ratios between pairs of species, \mathcal{X} and \mathcal{Y} , using their volume mixing ratios as defined in Equation 2. The abundance ratio is expressed in logarithmic

form as:

$$\begin{aligned} \log(\mathcal{X}/\mathcal{Y}) &:= \log_{10} \mathcal{X} - \log_{10} \mathcal{Y} \\ &:= \log_{10} \text{VMR}_{\mathcal{X}} - \log_{10} \text{VMR}_{\mathcal{Y}} \\ &:= \log_{10} \left(\frac{\text{VMR}_{\mathcal{X}}}{\text{VMR}_{\mathcal{Y}}} \right) \\ &:= \log_{10} \left(\frac{\mathcal{X}}{\mathcal{Y}} \right) \end{aligned} \quad (3)$$

We constrain the relative abundances for $\log(\text{H}^+/\text{Fe}) = -3.98^{+0.81}_{-1.14}$, $\log(\text{H}_2\text{O}/\text{CO}) = -1.23^{+1.00}_{-0.97}$, $\log(\text{CO}/\text{Fe}) = 1.04^{+0.80}_{-1.32}$, and $\log(\text{V}/\text{Fe}) = -3.56^{+0.66}_{-1.11}$ (Table 5, Figure 8). We now compare the retrieved abundance ratios with predictions from modelled equilibrium chemistry (Kitzmann et al. 2024). Overall, the retrieved abundance ratios are consistent with a $1 \times$ solar metallicity and a solar C/O ratio ($(\text{C}/\text{O})_{\odot} = 0.59 \pm 0.08$; Asplund et al. 2021).

The fraction of H₂O relative to CO (Figure 8, second panel) is 1 dex underabundant (sub-solar) than predictions from FastChem (but still consistent with solar within $1-\sigma$), likely due to water being partially dissociated into OH and O (Parmentier et al. 2018) at the high temperatures at play. This underabundance would be even more pronounced if assuming the stellar C/O rather than the solar C/O. We, indeed, retrieve a temperature $T = 2828^{+691}_{-238} \text{ K}$, assumed to be uniform across the atmosphere at the pressures probed, in agreement with Gandhi et al. (2023). At this temperature, the abundance of CO for a nearly-solar C/O remains unchanged. Therefore, according to Madhusudhan (2012), the $\log(\text{H}_2\text{O}/\text{CO})$ ratio is expected to be close to unity for a nearly-solar C/O ratio, in agreement with our retrieved abundance ratio ($\log(\text{H}_2\text{O}/\text{CO}) = -1.23^{+1.00}_{-0.97}$).

Intriguingly, the free retrieval constrains the abundance of H₂O despite the lack of a cross-correlation detection in our data (Figure 7, forth panel). This constraint is rather driven by the retrieval preferring to add water. In fact, H₂O has been detected in both high- and low-resolution observations (Evans et al. 2016;

Table 5: WASP-121b SCARLET atmospheric posteriors from the retrieval analysis on the HARPS, NIRPS, and CRIRES+ time series combined.

Parameters	Description	Value	Prior range
$\log_{10}\text{Fe}$	Volume mixing ratio of iron	$-6.33^{+0.99}_{-0.40}$	$\mathcal{U}(-12, 0)$
$\log_{10}\text{V}$	Volume mixing ratio of vanadium	$-9.89^{+0.52}_{-0.53}$	$\mathcal{U}(-12, 0)$
$\log_{10}\text{H}^-$	Volume mixing ratio of hydride	$-10.31^{+0.71}_{-0.60}$	$\mathcal{U}(-12, 0)$
$\log_{10}\text{e}^-$	Volume mixing ratio of electrons	$-6.08^{+3.22}_{-3.67}$	$\mathcal{U}(-12, 0)$
$\log_{10}\text{H}_2\text{O}$	Volume mixing ratio of water vapour	$-6.52^{+0.49}_{-0.68}$	$\mathcal{U}(-12, 0)$
$\log_{10}\text{CO}$	Volume mixing ratio of carbon monoxide	$-5.29^{+0.69}_{-0.87}$	$\mathcal{U}(-12, 0)$
$\log_{10}\text{TiO}$	Volume mixing ratio titanium oxide	$-11.18^{+0.66}_{-0.41}$	$\mathcal{U}(-12, 0)$
$\log_{10}\text{OH}$	Volume mixing ratio of hydroxyl	$-8.22^{+1.24}_{-2.52}$	$\mathcal{U}(-12, 0)$
T [K]	Atmospheric temperature	2828^{+691}_{-238}	$\mathcal{U}(100, 6000)$
K_p [km/s]	Planet velocity semi-amplitude	$202.99^{+2.84}_{-2.92}$	$\mathcal{U}(156, 276)$
V_{sys} [km/s]	Systemic velocity	$31.96^{+0.71}_{-0.69}$	$\mathcal{U}(18, 58)$
FWHM [km/s]	Rotational broadening FWHM	$6.20^{+1.40}_{-1.67}$	$\mathcal{U}(0, 20)$
$\log(\text{H}^-/\text{Fe})$	Relative abundance	$-3.98^{+0.81}_{-1.14}$	—
$\log(\text{V}/\text{Fe})$	Relative abundance	$-3.56^{+0.66}_{-1.11}$	—
$\log(\text{CO}/\text{Fe})$	Relative abundance	$1.04^{+0.80}_{-1.32}$	—
$\log(\text{H}_2\text{O}/\text{CO})$	Relative abundance	$-1.23^{+1.00}_{-0.97}$	—

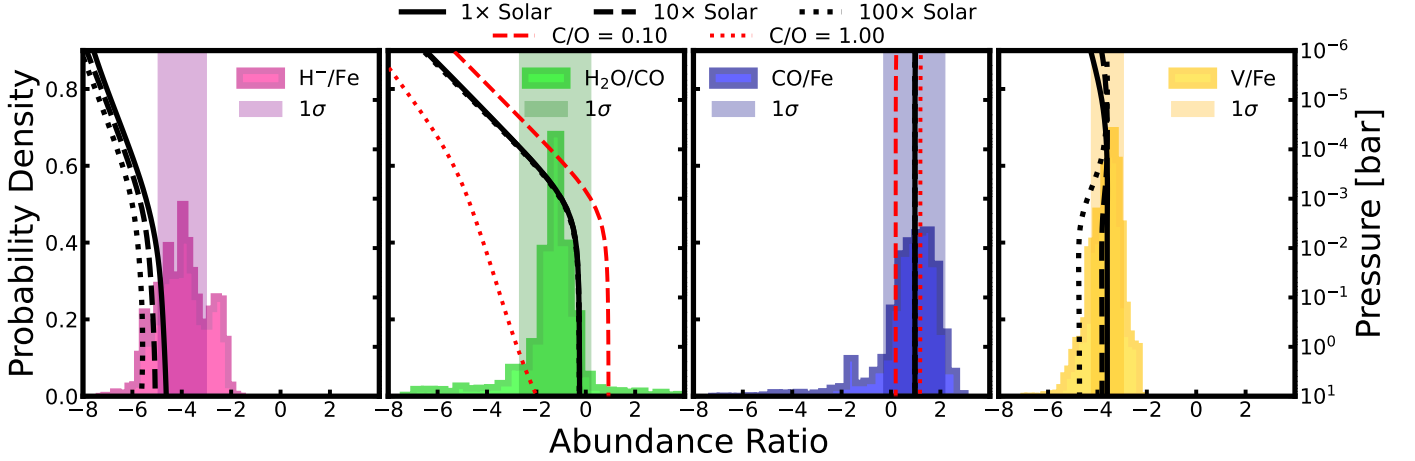


Fig. 8: Key retrieved results. The four distributions represent the probability density of retrieved chemical abundance ratios (in logarithmic scale). Overplotted the FastChem model predictions in chemical equilibrium as varying the metallicity and the C/O ratio. FastChem theoretical models are displayed as function of the pressure in bar.

Wardenier et al. 2024). Therefore, a non-detection in the cross-correlation space is more likely due to the limited sensitivity of our data rather than the absence of H_2O in WASP-121b atmosphere. Notably, Wardenier et al. (2024) reported a significant H_2O detection only after stacking three transits gathered with IGRINS installed on Gemini, a 8-m class telescope. The breaking up of water molecules is significant in ultra-hot gas giants, where it must be accounted for when inferring chemical abundances, especially in comparison to more thermally stable species like CO. Carbon monoxide is, indeed, a benchmark molecule to compare with (Parmentier et al. 2018; Savel et al. 2023). The reason is twofold: (i) due to its chemical robustness (thanks to the triple covalent bond), CO is less prone to thermal dissociation (via $\text{CO} \rightleftharpoons \text{C} + \text{O}$), thus remaining nearly constant with pressure (with the exception of known torrid exoplan-

ets with fully dissociated atmospheres, such as KELT-9b, Gaudi et al. 2017; Hoeijmakers et al. 2018); and, (ii) CO is also poorly sensitive to model assumptions on its abundance profile, being resistant to thermal dissociation. The $\log(\text{H}_2\text{O}/\text{CO})$ abundance ratio also serves as an indicator of the atmospheric region probed by our data, as well as of the dissociation and condensation of volatile compounds. Indeed, water condensates and dissociates more readily than CO for the reasons illustrated above. According to the retrieved quantity, which relies on model assumptions, and the chemistry predictions, we sample the pressure layer from sub-to-millibar ($\sim 10^{-4} - 10^{-3}$ bar), hence, we do not have access to the inflated upper atmosphere of WASP-121b, but rather we have insights to lower pressures.

We find that the retrieved $\log(\text{CO}/\text{Fe})$ ratio is consistent with the solar value (Figure 8, third panel), implying that the

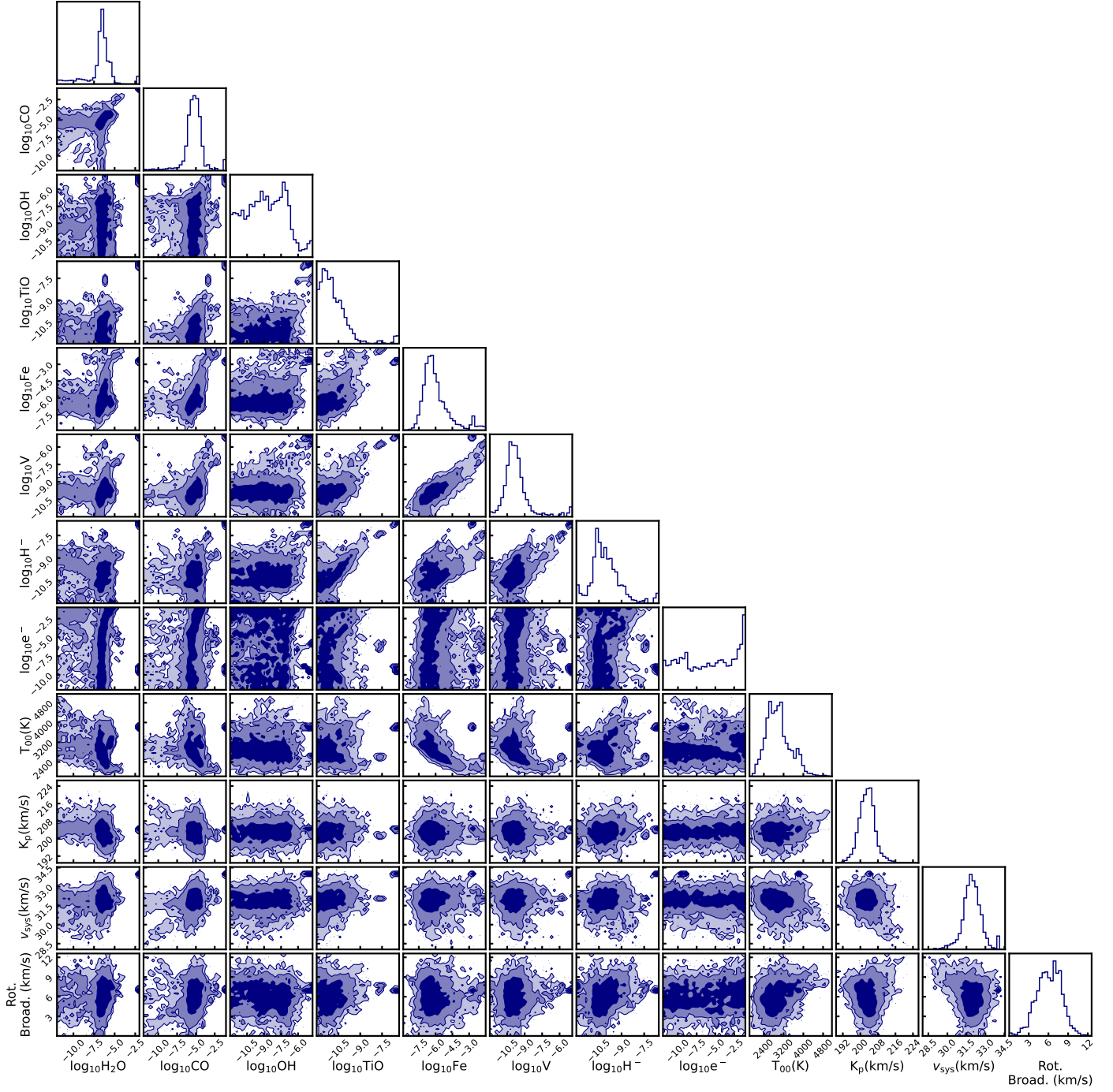


Fig. 9: Retrieved constraints on the atmospheric and orbital properties from HARPS, NIRPS and CRIRES+ combined transits of WASP-121b. We assume a free atmospheric retrieval condition, hence a well-mixed chemistry (constant-with-altitude).

planet’s atmosphere likely experiences moderate-to-high temperature, not extreme enough to dissociate CO molecules and not cool enough to allow extensive Fe rainout. The $\log(\text{CO}/\text{Fe})$ ratio can be also interpreted as a proxy of the volatile-to-refractory budget, i.e. the ice-to-rock ratio. Moreover, the $\log(\text{CO}/\text{Fe})$ ratio, being consistent with a model assuming a solar amount of carbon relative to oxygen, suggests that the atmosphere is not heavily skewed toward either a super-solar abundance of carbon or oxygen, but is instead chemically balanced. However, an atmosphere carrying a C/O ratio consistent-with-solar, likely favour a surplus of oxygen which is mostly bound in water molecules at low temperatures but which is set free by thermal dissocia-

tion of H_2O at high temperatures (as the case of ultra-hot gas giants) and pairs to form CO ($\text{CH}_4 + \text{H}_2\text{O} \rightleftharpoons \text{CO} + 3\text{H}_2$) and OH ($\text{H}_2\text{O} \rightleftharpoons 2\text{H} + \text{O}$) (Madhusudhan 2012).

The retrieved consistency with a C/O=solar contrasts with: (i) the carbon-enriched (volatile-enriched relative to refractory) atmosphere reported by Pelletier et al. (2024), which shows a super-solar C/O ratio ($\text{C/O} = 0.87^{+0.04}_{-0.06}$) from a free retrieval and a super-stellar ratio ($\text{C/O} = 0.73^{+0.07}_{-0.08}$) from a chemically consistent retrieval; and (ii) the super-stellar C/O ratio ($\text{C/O} = 0.70^{+0.07}_{-0.10}$) and a moderately super-stellar refractory-to-volatile ratio ($3.83^{+3.62}_{-1.67} \times \text{stellar}$) found by Smith et al. (2024) under

chemical equilibrium conditions. Despite both studies report elevated C/O ratios from dayside observations, [Pelletier et al. \(2024\)](#) favour a scenario enriched in ice-forming elements over rock-forming elements, suggesting the planet formed farther out in the disk beyond the ice-line, while [Smith et al. \(2024\)](#) suggest that WASP-121b likely formed between the soot line and the H₂O snow line ([Lothringer et al. 2021](#); [Chachan et al. 2023](#)). Our finding places WASP-121b in the nearly chemically balanced regime, not markedly favouring either a volatile-rich or refractory-rich formation environment. However, it is worth noticing that our results based on transit time-series rather than dayside observations, thus our data probe a different altitude in the atmosphere of WASP-121b.

We retrieve a $\log(V/\text{Fe})$ ratio that is consistent with chemical models assuming a solar composition (Figure 8, forth panel) indicating that the refractory balance is preserved in the atmosphere of WASP-121b, fully in agreement with equilibrium chemistry predictions. Our retrieved elemental ratio is also well consistent with that of [Maguire et al. \(2023\)](#) (see their Figure 4, second panel), based on three transits observed with ESPRESSO/VLT and fully in agreement with one UVES transit used as a benchmark.

The measured $\log(\text{H}^-/\text{Fe})$ ratio (Figure 8, first panel) can be a tracer of both the opacity contribution from H⁻ in the (near-)infrared regime, and the ionisation processes involving the electron density associated with the ionisation of metals, which are the primary source of free electrons ([Bell & Berrington 1987](#); [John 1988](#)).

The retrieval fails to constrain the abundance of free electrons (Figure 9), likely due to either the spectral range of our observations does not extend to wavelengths sensitive to the free-free transitions to form H⁻, or the inefficiency of metal ionisation within the pressure and temperature regime probed by the data. H⁻ bound-free absorption can dominate the spectrum below $\sim 1.6 \mu\text{m}$, masking spectral features from species such as H₂O and TiO. Similarly, the retrieval sets an upper limit for TiO, despite also non-detected in cross-correlation. Nevertheless, caution is warranted, as the line list used for TiO may lack the accuracy required to draw firm conclusions about the presence of TiO in the atmosphere of WASP-121b ([Prinoth et al. 2025](#)). However, [Prinoth et al. \(2025\)](#) reported a significant detection of Ti (albeit at a weaker strength than expected) in high signal-to-noise optical transits, suggesting that TiO may also be present.

In ultra-hot gas giants, ionisation involves both thermal processes and photoionisation ([Kitzmann et al. 2018](#); [Fossati et al. 2020](#)). However, the effects of the latter is not considered in the equilibrium chemistry models. Hence, the modelled $\log(\text{H}^-/\text{Fe})$ profile primarily reflects thermally driven ionisation processes occurring in WASP-121b at (sub-)millibar pressures. In this context, the measured $\log(\text{H}^-/\text{Fe})$ is consistent with FastChem models of a solar composition, and function as a thermometer in thermal equilibrium atmospheres according to the Saha ionisation equation ([Saha 1920](#)). Even though the retrieved elemental hydride-to-Fe ratio is consistent with model predictions within 1σ , the median of the Gaussian distribution peaks at marginally super-solar values, hinting at either an elevated abundance of hydride continuum opacity similar to what found in WASP-189b ([Vaulato et al. 2025](#)) but likely to compensate for missing opacity contributions in the model assumption, or a depleted Fe content due to condensation. The atmosphere of WASP-121b boasts a wealth of detected chemical species (see Section 1 for a complete literature overview) which we decided not to include in our atmospheric retrieval calculation and model. The main reason behind our choice is computational limitations.

Therefore, H⁻ is supposedly overcompensating for other missing opacity sources from species not included in our model. Indeed, the continuum should be handled mainly by the hydride and so by the density of free-electrons (e⁻), which have proven to be the principal continuum absorbers, particularly in ultra-hot gas giants ([Parmentier et al. 2018](#); [Arcangeli et al. 2018](#); [Vaulato et al. 2025](#)). We also surmise that photoionisation mechanisms might become relevant since the $\log(\text{H}^-/\text{Fe})$ ratio peaks at about 10^{-4} , higher than predicted by solar chemical equilibrium models (10^{-5}). Nevertheless, the retrieved $\log(\text{H}^-/\text{Fe})$ abundance ratio results consistent with solar models within 1 dex.

5.3. Orbital velocities

We retrieve a systemic velocity of $V_{\text{sys}} = 31.96_{-0.69}^{+0.71} \text{ km s}^{-1}$. We also constrain an orbital velocity of $K_p = 202.99_{-2.92}^{+2.84} \text{ km s}^{-1}$.

Leveraging the largest radial velocity dataset of WASP-121b to date, we update the orbital parameters, deriving the orbital velocity K_p from the stellar reflex motion obtained via the *juliet* fitting routine, as detailed in Section 3. By comparing our derived orbital velocities from both the RV analysis and the atmospheric retrieval routine, we calculate the velocity offset, ΔK_p^3 ([Wardenier et al. 2025](#)), which reflects the rate of change of the Doppler shift of the planetary signal across the orbital phases from (0,0) km s^{-1} in the planet rest frame. By inspecting the $K_p - V_{\text{sys}}$ maps, the planetary signal appears overall diffused (not a point-like source), likely due to dynamics and 3D effects, which are modelled as one free rotational broadening parameter in the atmospheric retrieval and retrieved to be $6.20_{-1.67}^{+1.40} \text{ km s}^{-1}$, consistent with the expectations. Transmission data are generally more sensitive to atmospheric dynamics, hence, we could expect a rotational broadening parameter that slightly differs from the planet rotation rate⁴. The retrieved rotational broadening parameter is not significantly under or over-broadened, thus ruling out potential resolution biases. In case of Fe, V and CO, the signal-to-noise ratio peaks at both lower K_p and lower V_{sys} values (see Figure 7) than the reference ones, resulting in blueshifted signals along the radial velocity axis and a change in slope (i.e. acceleration) along the the orbital velocity axis. These results can be contextualized within the framework proposed by [Wardenier et al. \(2023, 2024\)](#) who present detailed three-dimensional global circulation models for WASP-121b, and simulate the resulting high-resolution transmission spectra across different dynamical regimes. We consider four GCMs (see Figure 10): the first is a drag-free ($\tau_{\text{drag}} \rightarrow \infty$) model illustrated in [Parmentier et al. \(2018\)](#), while the other three models are presented in [Tan et al. \(2024\)](#) including one drag-free ($\tau_{\text{drag}} \rightarrow \infty$) model, one weak-drag model ($\tau_{\text{drag}} = 10^6 \text{ s}$), and one with a strong-drag prediction ($\tau_{\text{drag}} = 10^4 \text{ s}$), where τ is the uniform drag timescale. The drag-timescale variable represents the time needed for a parcel of air to lose a substantial percentage of its kinetic energy. It describes the wind speed, thus the efficiency of heat redistribution, and the Doppler shifts observed in the spectra. The zero-drag model accounts for a super-rotating equatorial jet ([Wardenier et al. 2021](#)), while jet formation is suppressed in the drag-models. Indeed, in both weak- and strong-drag models, the wind profile is mainly dominated by day-to-night flows. Moreover, the day-to-night contrast is preserved in all models being the

³ $\Delta K_p = K_p^{\text{retrieved}} - K_p^{\text{orbital}}$

⁴ $v_{\text{eq. rot.}} = \omega \times R_p = (2\pi/P) \times R_p \approx 6.86 \text{ km s}^{-1}$, where $\omega = 2\pi/P$ is the angular velocity, P is WASP-121b orbital period estimated with the *juliet* RV fitting carried out in this work (see Table 4), and R_p is the planet radius.

planet tidally locked. Therefore, these global circulation models demonstrate that the presence, or absence, of atmospheric drag strongly modulates the Doppler shift of the planetary signal. In particular, drag-free models naturally produce a symmetric latitudinal temperature structure and high longitudinal temperature gradients at the terminator (strong day-to-night temperature variations), resulting in measurable Doppler shifts in the planetary trail due to winds and rotation. Indeed, the changing and evolving structure of the planet’s atmosphere as viewed at different phases results in a variation of the position of the planet’s spectral lines, eventually resulting in a measurable shift in the K_p . This is consistent with our detection of a negative ΔK_p and ΔV_{sys} for Fe, V and CO. Indeed, GCMs predict a decrease in the observed K_p , specifically producing a negative ΔK_p , regardless of the drag.

However, as highlighted in Table 6 and Figure 10, the calculation of ΔK_p is sensitive to the assumed stellar mass, which feeds directly into the derived orbital velocity. Differences in M_\star lead to non-negligible changes in the interpretation of the Doppler shift and, therefore, in how well our observations align with specific GCM predictions. This emphasizes the importance of using consistent stellar parameters when comparing observationally derived kinematic shifts to model outputs.

WASP-121 is known as an hot, F6-type star, with a moderate chromospheric stellar activity level ($\log R'_{\text{HK}} \approx -4.8$ measured by Borsa et al. 2021). Bourrier et al. (2020) also reported on magnetically active regions at the surface of WASP-121, visible in the periodogram of the RV residuals (see their Figure 3). Moreover, the moderate-to-fast rotation of WASP-121 ($v \sin(i) = 11.90 \pm 0.31 \text{ km s}^{-1}$, Borsa et al. 2021) broadens the few stellar spectral lines typical of A- and F-type stars, blending lines that are usually isolated and more “peaky” in cold and slow rotating stars. As a result, deriving the chemical composition of these stars (e.g. the metallicity) becomes challenging and thus extracting stellar parameters such as the stellar mass is more difficult. Figure 10 clearly illustrates the variation in the computed ΔK_p as function of the stellar mass, but using the stellar reflex motion obtained from the radial velocity fitting in all four scenarios presented. Vertical lines mark the ΔK_p values predicted by GCMs. We can surely claim that all computed planet’s orbital velocity are consistent with either weak-drag or drag-free models, while the strong-drag configuration is ruled out, regardless of the model. These results are fully consistent with Warde-
nier et al. (2024).

Table 6: Mass reference. ΔK_p computed assuming different stellar masses by keeping fixed the stellar reflex motion.

Reference	$M_\star [M_\odot]$	$\Delta K_p [\text{km s}^{-1}]$
Delrez et al. (2016)	1.35 ± 0.08	-14 ± 5
Borsa et al. (2021)	1.38 ± 0.02	-15 ± 3
Sing et al. (2024)	1.33 ± 0.02	-13 ± 3
Prinoth et al. (2025)	1.42 ± 0.03	-18 ± 3

6. Conclusions

In this work, we present an atmospheric retrieval analysis of the ultra-hot Jupiter WASP-121b by combining high-resolution transmission spectra from HARPS, NIRPS, and CRRES+ (both K and H photometric bands). Leveraging the large high-resolution dataset, we constrain the planet’s atmospheric com-

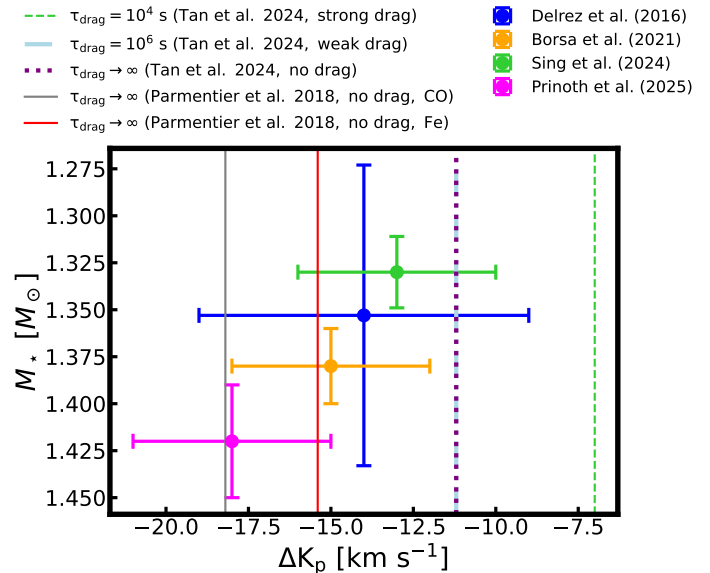


Fig. 10: ΔK_p as function of different stellar masses. This plot serves to visualize the Table 6 in comparison with global circulation model predictions. Each data point with uncertainties correspond to the computed ΔK_p as function of the stellar mass (reported in Table 6) as derived by Delrez et al. (2016) ($M_\star = 1.35 \pm 0.08 M_\odot$), Borsa et al. (2021) ($M_\star = 1.38 \pm 0.02 M_\odot$), Sing et al. (2024) ($M_\star = 1.33 \pm 0.02 M_\odot$), Prinoth et al. (2025) ($M_\star = 1.42 \pm 0.03 M_\odot$), respectively. Uncertainties are calculated via error propagation. Vertical lines mark the GCMs predictions, namely models with zero, weak and strong drag by Tan et al. (2024), and drag-free models by Parmentier et al. (2018).

position and orbital dynamics through a free retrieval approach using the SCARLET code.

We report the retrieved relative chemical abundances of key species, including Fe, V, CO, H_2O , OH, TiO, H^- , and e^- . While absolute abundances remain highly model-dependent and less informative, abundance ratios offer a more robust window into the atmospheric processes and underlying chemistry. Our results indicate that the atmosphere of WASP-121b is broadly consistent with a solar metallicity and a solar C/O ratio. This suggests that chemical equilibrium remains largely preserved at the pressure levels probed ($\sim 10^{-4}$ – 10^{-3} bar), with no strong evidence for substantial alteration from disequilibrium processes such as rainout, photochemistry, or deep vertical mixing.

Notably, we constrain the $\log(\text{H}_2\text{O}/\text{CO})$ ratio to be 1 dex sub-solar compared to chemical equilibrium predictions from FastChem, a result consistent with partial water dissociation at high temperatures. Despite the lack of a direct cross-correlation detection of H_2O , the retrieval favours the inclusion of water vapour to reproduce the observed spectra. The retrieved temperature of $2861^{+396}_{-418} \text{ K}$ reinforces the expectation of thermal dissociation affecting volatile species, such as water.

The $\log(\text{CO}/\text{Fe})$ and $\log(\text{V}/\text{Fe})$ ratios are in agreement with solar values, indicating that refractory-to-volatile balances are maintained and that CO remains stable against dissociation, consistent with its high bond energy. These findings reinforce the utility of CO as a chemically robust reference molecule in high-temperature atmospheres. In contrast, $\log(\text{H}^-/\text{Fe})$ emerges as a potentially sensitive tracer of thermal ionisation. The retrieval returns a value 1 dex elevated (but still within 1σ) compared

to solar predictions, hinting at either an elevated abundance of hydride continuum opacity but likely to compensate for missing opacity contributions in the model assumption, or a depleted Fe content due to condensation. However, the retrieval fails to constrain the electron density, limiting our ability to distinguish between enhanced H^- opacity and Fe depletion through condensation.

Intriguingly, the cross-correlation signals for Fe, V, and CO appear blueshifted along the radial velocity axis and peak at a lower orbital velocity than the reference one in K_p - V_{sys} space, suggesting the presence of equatorial winds and rotational broadening. These results are potentially indicative of drag-free or weak-drag atmospheric circulation as predicted by global circulation models. These models support a scenario in which CO probes higher-altitude layers subject to faster wind speeds, while Fe and V trace deeper regions where rotation dominates.

We also re-examine the planet's orbital parameters using the largest radial velocity dataset to date. We report on a global fit to radial velocity measurements (from CORALIE, HARPS, NIRPS, and ESPRESSO observations) and photometric light curves from TESS in order to refine the planetary orbital parameters. Indeed, thanks to the broad radial velocity dataset, the orbital parameters of the system are improved. By comparing the derived orbital velocity from both the radial velocity analysis and the atmospheric retrieval, we estimate the velocity offset, ΔK_p , and find it is non-zero, but consistent with predictions from either drag-free or weak-drag 3D global circulation models, while cautioning the non-negligible dependence on the stellar mass assumed.

Overall, our results provide a chemically and dynamically coherent picture of WASP-121b's atmosphere. The planet's bulk composition appears largely unaltered by disequilibrium processes, while local deviations—such as water dissociation and thermal ionisation—highlight the complexity of atmospheric processes in ultra-hot environments. This study demonstrates the power of combining multi-instrument high-resolution datasets with retrieval techniques to simultaneously probe chemical composition and atmospheric dynamics.

Future work will benefit from improved opacity databases—especially for TiO—and more physically complete models incorporating vertical mixing, photochemistry, and cloud condensation. The integration of low- and high-resolution datasets within a joint retrieval framework will be essential to further refine molecular abundance constraints.

Acknowledgements. This work has been carried out within the framework of the NCCR PlanetS supported by the Swiss National Science Foundation under grants 51NF40_182901 and 51NF40_205606.

RA acknowledges the Swiss National Science Foundation (SNSF) support under the Post-Doc Mobility grant P500PT_222212 and the support of the Institut Trottier de Recherche sur les Exoplanètes (IREx).

RA, JPW, ÉA, FBa, BB, NJC, RD, LMa & CC acknowledge the financial support of the FRQ-NT through the Centre de recherche en astrophysique du Québec as well as the support from the Trottier Family Foundation and the Trottier Institute for Research on Exoplanets.

ML, HC & BA acknowledge support of the Swiss National Science Foundation under grant number PCEFP2_194576.

DE and MS acknowledge support from the Swiss National Science Foundation for project 200021_200726.

VV, SP, DE, & MS acknowledge the financial support of the SNSF.

NN, JIGH, RR, ASM & AKS acknowledge financial support from the Spanish Ministry of Science, Innovation and Universities (MICIU) projects PID2020-117493GB-I00 and PID2023-149982NB-I00.

NN acknowledges financial support by Light Bridges S.L, Las Palmas de Gran Canaria.

NN acknowledges funding from Light Bridges for the Doctoral Thesis "Habitable Earth-like planets with ESPRESSO and NIRPS", in cooperation with the Instituto de Astrofísica de Canarias, and the use of Indefeasible Computer Rights (ICR) being commissioned at the ASTRO POC project in the Island of Tenerife,

Canary Islands (Spain). The ICR-ASTRONOMY used for his research was provided by Light Bridges in cooperation with Hewlett Packard Enterprise (HPE). XDü acknowledges the support from the European Research Council (ERC) under the European Union's Horizon 2020 research and innovation programme (grant agreement SCORE No 851555) and from the Swiss National Science Foundation under the grant SPECTRE (No 200021_215200).

This work was supported by grants from eSSENCE (grant number eSSENCE@LU 9:3), the Swedish National Research Council (project number 2023 05307), The Crafoord foundation and the Royal Physiographic Society of Lund, through The Fund of the Walter Gyllenberg Foundation."

ÉA, FBa, RD & LMa acknowledges support from Canada Foundation for Innovation (CFI) program, the Université de Montréal and Université Laval, the Canada Economic Development (CED) program and the Ministère of Economy, Innovation and Energy (MEIE).

SCB, ED-M, NCS & ARCS acknowledge the support from FCT - Fundação para a Ciência e a Tecnologia through national funds by these grants: UIDB/04434/2020, UIDP/04434/2020.

SCB acknowledges the support from Fundação para a Ciência e Tecnologia (FCT) in the form of a work contract through the Scientific Employment Incentive program with reference 2023.06687.CEECIND and DOI 10.54499/2023.06687.CEECIND/CP2839/CT0002.

XB, XDe & TF acknowledge funding from the French ANR under contract number ANR24CE493397 (ORVET), and the French National Research Agency in the framework of the Investissements d'Avenir program (ANR-15-IDEX-02), through the funding of the "Origin of Life" project of the Grenoble-Alpes University.

The Board of Observational and Instrumental Astronomy (NAOS) at the Federal University of Rio Grande do Norte's research activities are supported by continuous grants from the Brazilian funding agency CNPq. This study was partially funded by the Coordenação de Aperfeiçoamento de Pessoal de Nível Superior—Brasil (CAPES) — Finance Code 001 and the CAPES-Print program. BLCM acknowledge CAPES postdoctoral fellowships.

BLCM acknowledges CNPq research fellowships (Grant No. 305804/2022-7).

NBC acknowledges support from an NSERC Discovery Grant, a Canada Research Chair, and an Arthur B. McDonald Fellowship, and thanks the Trottier Space Institute for its financial support and dynamic intellectual environment.

JRM acknowledges CNPq research fellowships (Grant No. 308928/2019-9).

ED-M further acknowledges the support from FCT through Stimulus FCT contract 2021.01294.CEECIND. ED-M acknowledges the support by the Ramón y Cajal contract RyC2022-035854-I funded by MICIU/AEI/10.13039/501100011033 and by ESF+.

ICL acknowledges CNPq research fellowships (Grant No. 313103/2022-4).

CMo acknowledges the funding from the Swiss National Science Foundation under grant 200021_204847 "PlanetsInTime".

Co-funded by the European Union (ERC, FIERCE, 101052347). Views and opinions expressed are however those of the author(s) only and do not necessarily reflect those of the European Union or the European Research Council. Neither the European Union nor the granting authority can be held responsible for them.

GAW is supported by a Discovery Grant from the Natural Sciences and Engineering Research Council (NSERC) of Canada.

0

KAM acknowledges support from the Swiss National Science Foundation (SNSF) under the Postdoc Mobility grant P500PT_230225.

ARCS acknowledges the support from Fundação para a Ciência e a Tecnologia (FCT) through the fellowship 2021.07856.BD.

BP acknowledges financial support from the Walter Gyllenberg Foundation.

AKS acknowledges financial support from La Caixa Foundation (ID 100010434) under the grant LCF/BQ/DI23/11990071.

BT acknowledges the financial support from the Wenner-Gren Foundation (WGF2022-0041).

AP acknowledges support from the Unidad de Excelencia María de Maeztu CEX2020-001058-M programme and from the Generalitat de Catalunya/CERCA.

References

- Anderson, D. R., Temple, L. Y., Nielsen, L. D., et al. 2018, arXiv:1809.04897 [astro-ph], arXiv: 1809.04897
- Arcangeli, J., Désert, J.-M., Line, M. R., et al. 2018, ApJ Letters, 855, L30
- Arcangeli, J., Désert, J.-M., Parmentier, V., et al. 2019, A&A, 625, A136, publisher: EDP Sciences
- Asplund, M., Amarsi, A. M., & Grevesse, N. 2021, A&A, 653, A141
- Bazin, L., Allart, R., Benneke, B., et al. 2025, arXiv e-prints, arXiv:2508.06626
- Bazin, L., Pelletier, S., Benneke, B., Salinas, R., & Mace, G. N. 2024, The Astronomical Journal, 167, 206

- Bell, K. L. & Berrington, K. A. 1987, *Journal of Physics B: Atomic and Molecular Physics*, 20, 801
- Bell, T. J. & Cowan, N. B. 2018, *ApJ*, 857, L20
- Benneke, B. 2015, [arXiv:1504.07655](https://arxiv.org/abs/1504.07655)
- Benneke, B., Cowan, N., Rowe, J., et al. 2019, *Exoplanet instrumentation in the 2020s: Canada's pathway towards searching for life on potentially Earth-like exoplanets*, Tech. rep., Zenodo
- Benneke, B. & Seager, S. 2012, *ApJ*, 753, 100
- Benneke, B. & Seager, S. 2013, *ApJ*, 778, 153
- Birkby, J. L., Kok, D., J. R., et al. 2013, *MNRAS: Letters*, 436, L35
- Borsa, F., Allart, R., Casasayas-Barris, N., et al. 2021, *A&A*, 645, A24
- Borysow, A. 2002, *A&A*, 390, 779
- Bouchy, F., Doyon, R., & Francesco, P. 2025
- Bourrier, V., Ehrenreich, D., Lendl, M., et al. 2020, *A&A*, 635, A205
- Broeg, C., Fernández, M., & Neuhäuser, R. 2005, *Astronomische Nachrichten*, 326, 134
- Broggi, M. & Line, M. R. 2019, *The Astronomical Journal*, 157, 114
- Broggi, M., Snellen, I. A. G., de Kok, R. J., et al. 2012, *Nature*, 486, 502
- Burningham, B., Marley, M. S., Line, M. R., et al. 2017, *MNRAS*, 470, 1177
- Casasayas-Barris, N., Borsa, F., Palle, E., et al. 2022, *A&A*, 664, A121
- Chachan, Y., Knutson, H. A., Lothringer, J., & Blake, G. A. 2023, *ApJ*, 943, 112
- Chakraborty, H., Lendl, M., Akisanmi, B., Petit dit de la Roche, D. J. M., & Deline, A. 2024, *A&A*, 685, A173
- Collier Cameron, A., Guenther, E., Smalley, B., et al. 2010, *MNRAS*, 407, 507
- Cutri, R. M., Skrutskie, M. F., van Dyk, S., et al. 2003, *VizieR Online Data Catalog: 2MASS All-Sky Catalog of Point Sources (Cutri+ 2003)*, VizieR On-line Data Catalog: II/246. Originally published in: University of Massachusetts and Infrared Processing and Analysis Center, (IPAC/California Institute of Technology) (2003)
- Dekker, H., D'Odorico, S., Kaufer, A., Delabre, B., & Kotzlowski, H. 2000, in *Society of Photo-Optical Instrumentation Engineers (SPIE) Conference Series*, Vol. 4008, *Optical and IR Telescope Instrumentation and Detectors*, ed. M. Iye & A. F. Moorwood, 534–545
- Delrez, L., Santerne, A., Almenara, J.-M., et al. 2016, *MNRAS*, 458, 4025
- Dorn, R. J., Bristow, P., Smoker, J. V., et al. 2023, *A&A*, 671, A24, publisher: EDP Sciences
- Ehrenreich, D., Lovis, C., Allart, R., et al. 2020, *Nature*, 580, 597
- Espinoza, N., Kossakowski, D., & Brahm, R. 2019, *MNRAS*, 490, 2262
- Evans, T. M., Sing, D. K., Wakeford, H. R., et al. 2016, *ApJ*, 822, L4
- Evans-Soma, T. M., Sing, D. K., Barstow, J. K., et al. 2025, *Nature Astronomy* [[arXiv:2506.01771](https://arxiv.org/abs/2506.01771)]
- Follert, R., Dorn, R. J., Oliva, E., et al. 2014, in *Ground-based and Airborne Instrumentation for Astronomy V*, Vol. 9147 (International Society for Optics and Photonics), 914719
- Foreman-Mackey, D., Agol, E., Ambikasaran, S., & Angus, R. 2017, *AJ*, 154, 220
- Foreman-Mackey, D., Hogg, D. W., Lang, D., & Goodman, J. 2013, *Publications of the Astronomical Society of the Pacific*, 125, 306
- Fossati, L., Shulyak, D., Sreejith, A. G., et al. 2020, *A&A*, 643, A131
- Fulton, B. J., Petigura, E. A., Blunt, S., & Sinukoff, E. 2018, *PASP*, 130, 044504
- Gandhi, S., Kesseli, A., Zhang, Y., et al. 2023, *The Astronomical Journal*, 165, 242
- Gandhi, S., Kesseli, A., Zhang, Y., et al. 2023, *AJ*, 165, 242
- Gapp, C., Evans-Soma, T. M., Barstow, J. K., et al. 2025, *AJ*, 169, 341
- Garcia, L. J., Timmermans, M., Pozuelos, F. J., et al. 2022, *MNRAS*, 509, 4817
- Gaudi, B. S., Stassun, K. G., Collins, K. A., et al. 2017, *Nature*, 546, 514
- Gibson, N. P., Merritt, S., Nugroho, S. K., et al. 2020, *MNRAS*, 493, 2215
- Gibson, N. P., Nugroho, S. K., Lothringer, J., Maguire, C., & Sing, D. K. 2022, *MNRAS*, 512, 4618
- Gray, D. F. 2021, *The Observation and Analysis of Stellar Photospheres* (4th ed.), cambridge: Cambridge University Press.
- Grimm, S. L. & Heng, K. 2015, *ApJ*, 808, 182
- Grimm, S. L., Malik, M., Kitzmann, D., et al. 2021, *ApJ Supplement Series*, 253, 30
- Hellier, C., Anderson, D. R., Cameron, A. C., et al. 2009, *Nature*, 460, 1098
- Hellier, C., Lewis, D., Samra, D., et al. 2021, *A&A*, 649, A44
- Hobson, M. J., Bouchy, F., Lavie, B., et al. 2024, *A&A*, 688, A216
- Hoeijmakers, H. J., Cabot, S. H. C., Zhao, L., et al. 2020a, *A&A*, 641, A120
- Hoeijmakers, H. J., Ehrenreich, D., Heng, K., et al. 2018, *Nature*, 560, 453
- Hoeijmakers, H. J., Ehrenreich, D., Kitzmann, D., et al. 2019, *A&A*, 627, A165
- Hoeijmakers, H. J., Kitzmann, D., Morris, B. M., et al. 2024, *A&A*, 685, A139
- Hoeijmakers, H. J., Seidel, J. V., Pino, L., et al. 2020b, *A&A*, 641, A123
- Høg, E., Fabricius, C., Makarov, V. V., et al. 2000, *A&A*, 355, L27
- Jenkins, J. M., Twicken, J. D., McCaulliff, S., et al. 2016, in *Society of Photo-Optical Instrumentation Engineers (SPIE) Conference Series*, Vol. 9913, *Software and Cyberinfrastructure for Astronomy IV*, ed. G. Chiozzi & J. C. Guzman, 99133E
- John, T. L. 1988, *Astronomy and Astrophysics*, 193, 189
- Juvan, I. G., Lendl, M., Cubillos, P. E., et al. 2018, *A&A*, 610, A15
- Kipping, D. M. 2013, *MNRAS*, 435, 2152
- Kitzmann, D., Heng, K., Rimmer, P. B., et al. 2018, *ApJ*, 863, 183
- Kitzmann, D., Stock, J. W., & Patzer, A. B. C. 2024, *MNRAS*, 527, 7263
- Kreidberg, L. 2015, *PASP*, 127, 1161
- Lendl, M., Anderson, D. R., Collier-Cameron, A., et al. 2012, *A&A*, 544, A72
- Lendl, M., Cubillos, P. E., Hagelberg, J., et al. 2017, *A&A*, 606, A18
- Li, G., Gordon, I. E., Rothman, L. S., et al. 2015, *ApJ Supplement Series*, 216, 15
- Lothringer, J. D., Barman, T., & Koskinen, T. 2018, *ApJ*, 866, 27
- Lothringer, J. D., Rustamkulov, Z., Sing, D. K., et al. 2021, *ApJ*, 914, 12
- Lund, M. B., Rodriguez, J. E., Zhou, G., et al. 2017, *The Astronomical Journal*, 154, 194
- Madhusudhan, N. 2012, *ApJ*, 758, 36
- Maguire, C., Gibson, N. P., Nugroho, S. K., et al. 2023, *MNRAS*, 519, 1030
- McKemmish, L. K., Masseron, T., Hoeijmakers, H. J., et al. 2019, *MNRAS*, 488, 2836
- Merritt, S. R., Gibson, N. P., Nugroho, S. K., et al. 2021, *MNRAS*, 506, 3853
- Park, C., Jaffe, D. T., Yuk, I.-S., et al. 2014, in *Ground-based and Airborne Instrumentation for Astronomy V*, Vol. 9147 (SPIE), 510–521
- Parmentier, V., Line, M. R., Bean, J. L., et al. 2018, *A&A*, 617, A110
- Patel, J. A. & Espinoza, N. 2022, *The Astronomical Journal*, 163, 228
- Pelletier, S., Benneke, B., Ali-Dib, M., et al. 2023, *Nature*, 619, 491
- Pelletier, S., Benneke, B., Chachan, Y., et al. 2024, *The Astronomical Journal*, 169, 10
- Pelletier, S., Benneke, B., Darveau-Bernier, A., et al. 2021, *The Astronomical Journal*, 162, 73
- Pepe, F., Cristiani, S., Rebolo, R., et al. 2021, *A&A*, 645, A96
- Pepe, F., Mayor, M., Delabre, B., et al. 2000, in *Optical and IR Telescope Instrumentation and Detectors*, Vol. 4008 (SPIE), 582–592
- Polyansky, O. L., Kyuberis, A. A., Zobov, N. F., et al. 2018, *MNRAS*, 480, 2597
- Prinath, B., Hoeijmakers, H. J., Kitzmann, D., et al. 2022, *Nature Astronomy*, 6, 449
- Prinath, B., Hoeijmakers, H. J., Pelletier, S., et al. 2023, *A&A*, 678, A182
- Prinath, B., Seidel, J. V., Hoeijmakers, H. J., et al. 2025, *A&A*, 694, A284
- Ramkumar, S., Gibson, N. P., Nugroho, S. K., Fortune, M., & Maguire, C. 2025, *A&A*, 695, A110
- Rothman, L. S., Gordon, I. E., Barber, R. J., et al. 2010, *Journal of Quantitative Spectroscopy and Radiative Transfer*, 111, 2139
- Ryabchikova, T., Piskunov, N., Kurucz, R. L., et al. 2015, *Physica Scripta*, 90, 054005
- Saha, M. N. 1920, *The London, Edinburgh, and Dublin Philosophical Magazine and Journal of Science*, 40, 472, publisher: Taylor & Francis _eprint: <https://doi.org/10.1080/14786441008636148>
- Santos, N. C., Cristo, E., Demangeon, O., et al. 2020, [arXiv:2011.03746](https://arxiv.org/abs/2011.03746) [astro-ph]
- Savel, A. B., Kempton, E. M.-R., Rauscher, E., et al. 2023, *ApJ*, 944, 99, publisher: The American Astronomical Society
- Seidel, J. V., Borsa, F., Pino, L., et al. 2023, *A&A*, 673, A125
- Seidel, J. V., Ehrenreich, D., Allart, R., et al. 2021, *A&A*, 653, A73
- Seidel, J. V., Ehrenreich, D., Pino, L., et al. 2020a, *A&A*, 633, A86
- Seidel, J. V., Ehrenreich, D., Wyttenbach, A., et al. 2019, *A&A*, 623, A166
- Seidel, J. V., Lendl, M., Bourrier, V., et al. 2020b, *A&A*, 643, A45
- Seidel, J. V., Prinath, B., Pino, L., et al. 2025, *Nature*, 639, 902
- Silva, T. A., Demangeon, O. D. S., Santos, N. C., et al. 2022, *A&A*, 666, L10, publisher: EDP Sciences
- Sing, D. K., Evans-Soma, T. M., Rustamkulov, Z., et al. 2024, *The Astronomical Journal*, 168, 231
- Sing, D. K., Fortney, J. J., Nikolov, N., et al. 2016, *Nature*, 529, 59
- Sing, D. K., Lavvas, P., Ballester, G. E., et al. 2019, *The Astronomical Journal*, 158, 91
- Smith, J. C., Stumpe, M. C., Van Cleve, J. E., et al. 2012, *PASP*, 124, 1000
- Smith, P. C. B., Sanchez, J. A., Line, M. R., et al. 2024, *The Astronomical Journal*, 168, 293
- Snellen, I. A. G., Kok, R. J. d., Mooij, E. J. W. d., & Albrecht, S. 2010, *Nature*, 465, 1049
- Speagle, J. S. 2020, *MNRAS*, 493, 3132
- Stock, J. W., Kitzmann, D., & Patzer, A. B. C. 2022, *MNRAS*, 517, 4070
- Stock, J. W., Kitzmann, D., Patzer, A. B. C., & Sedlmayr, E. 2018, *MNRAS*, 479, 865
- Stumpe, M. C., Smith, J. C., Catanzarite, J. H., et al. 2014, *PASP*, 126, 100
- Stumpe, M. C., Smith, J. C., Van Cleve, J. E., et al. 2012, *PASP*, 124, 985
- Tan, X. & Komacek, T. D. 2019, *ApJ*, 886, 26
- Tan, X., Komacek, T. D., Batalha, N. E., et al. 2024, *MNRAS*, 528, 1016
- Torres, G., Andersen, J., & Giménez, A. 2010, *A&A Rev.*, 18, 67
- Vaulato, V., Pelletier, S., Ehrenreich, D., et al. 2025, *A&A*, 700, A9
- Wardenier, J. P., Parmentier, V., Lee, E. K. H., & Line, M. R. 2025, [arXiv:2502.01606](https://arxiv.org/abs/2502.01606)
- Wardenier, J. P., Parmentier, V., Lee, E. K. H., Line, M. R., & Gharib-Nezhad, E. 2021, *MNRAS*, 506, 1258
- Wardenier, J. P., Parmentier, V., Line, M. R., & Lee, E. K. H. 2023, *MNRAS*, 525, 4942

Wardenier, J. P., Parmentier, V., Line, M. R., et al. 2024, Publications of the Astronomical Society of the Pacific, 136, 084403
 West, R. G., Heliier, C., Almenara, J.-M., et al. 2016, A&A, 585, A126

¹Observatoire de Genève, Département d’Astronomie, Université de Genève, Chemin Pegasi 51, 1290 Versoix, Switzerland

²Institut Trottier de recherche sur les exoplanètes, Département de Physique, Université de Montréal, Montréal, Québec, Canada

³Centre Vie dans l’Univers, Faculté des sciences de l’Université de Genève, Quai Ernest-Ansermet 30, 1205 Geneva, Switzerland

⁴Light Bridges S.L., Observatorio del Teide, Carretera del Observatorio, s/n Guimar, 38500, Tenerife, Canarias, Spain

⁵Instituto de Astrofísica de Canarias (IAC), Calle Vía Láctea s/n, 38205 La Laguna, Tenerife, Spain

⁶Departamento de Astrofísica, Universidad de La Laguna (ULL), 38206 La Laguna, Tenerife, Spain

⁷Division of Astrophysics, Department of Physics, Lund University, Box 118, SE-22100 Lund, Sweden

⁸Observatoire du Mont-Mégantic, Québec, Canada

⁹Instituto de Astrofísica e Ciências do Espaço, Universidade do Porto, CAUP, Rua das Estrelas, 4150-762 Porto, Portugal

¹⁰Departamento de Física e Astronomia, Faculdade de Ciências, Universidade do Porto, Rua do Campo Alegre, 4169-007 Porto, Portugal

¹¹Department of Earth, Planetary, and Space Sciences, University of California, Los Angeles, CA 90095, USA

¹²Univ. Grenoble Alpes, CNRS, IPAG, F-38000 Grenoble, France

¹³Department of Physics, University of Toronto, Toronto, ON M5S 3H4, Canada

¹⁴Departamento de Física Teórica e Experimental, Universidade Federal do Rio Grande do Norte, Campus Universitário, Natal, RN, 59072-970, Brazil

¹⁵Department of Physics & Astronomy, McMaster University, 1280 Main St W, Hamilton, ON, L8S 4L8, Canada

¹⁶Department of Physics, McGill University, 3600 rue University, Montréal, QC, H3A 2T8, Canada

¹⁷Department of Earth & Planetary Sciences, McGill University, 3450 rue University, Montréal, QC, H3A 0E8, Canada

¹⁸Centro de Astrobiología (CAB), CSIC-INTA, Camino Bajo del Castillo s/n, 28692, Villanueva de la Cañada (Madrid), Spain

¹⁹European Southern Observatory (ESO), Karl-Schwarzschild-Str. 2, 85748 Garching bei München, Germany

²⁰Space Research and Planetary Sciences, Physics Institute, University of Bern, Gesellschaftsstrasse 6, 3012 Bern, Switzerland

²¹Consejo Superior de Investigaciones Científicas (CSIC), E-28006 Madrid, Spain

²²Bishop’s University, Dept of Physics and Astronomy, Johnson-104E, 2600 College Street, Sherbrooke, QC, Canada, J1M 1Z7, Canada

²³Department of Physics, Engineering Physics, and Astronomy, Queen’s University, 99 University Avenue, Kingston, ON K7L 3N6, Canada

²⁴Department of Physics and Space Science, Royal Military College of Canada, 13 General Crerar Cres., Kingston, ON K7P 2M3, Canada

²⁵School of Mathematical and Physical Sciences, Macquarie University, Sydney, NSW 2109, Australia

²⁶Lund Observatory, Division of Astrophysics, Department of Physics, Lund University, Box 118, 221 00 Lund, Sweden

²⁷European Southern Observatory (ESO), Av. Alonso de Cordova 3107, Casilla 19001, Santiago de Chile, Chile

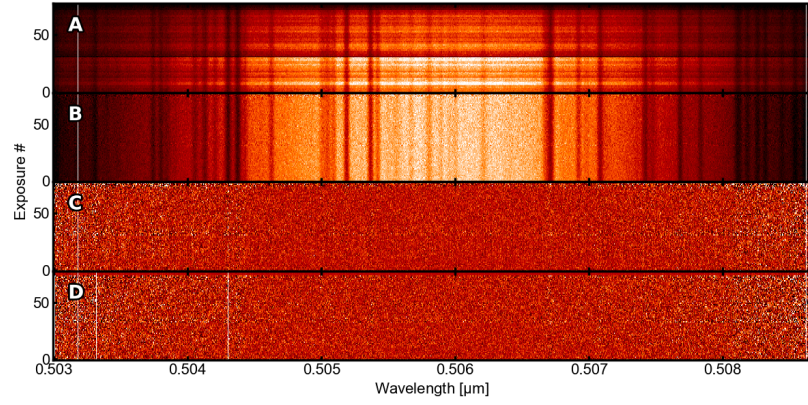
²⁸Université Côte d’Azur, Observatoire de la Côte d’Azur, CNRS, Laboratoire Lagrange, 06000 Nice, France

²⁹Institute of Space Sciences (ICE, CSIC), Carrer de Can Magrans S/N, Campus UAB, Cerdanyola del Valles, E-08193, Spain

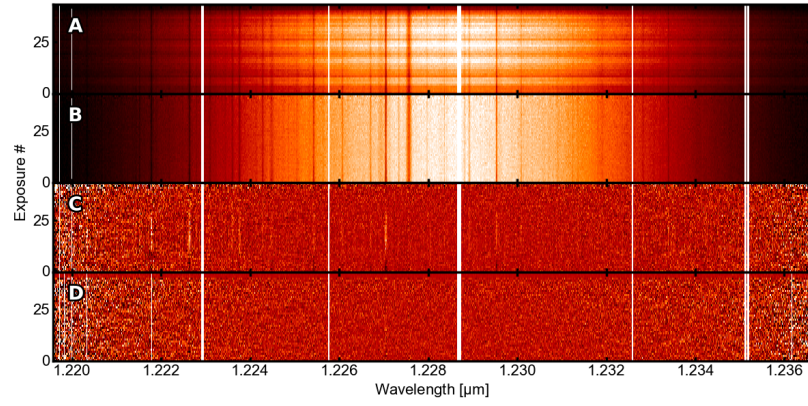
³⁰Institut d’Estudis Espacials de Catalunya (IEEC), 08860 Castelldefels (Barcelona), Spain

*e-mail: valentina.vaulato@unige.ch

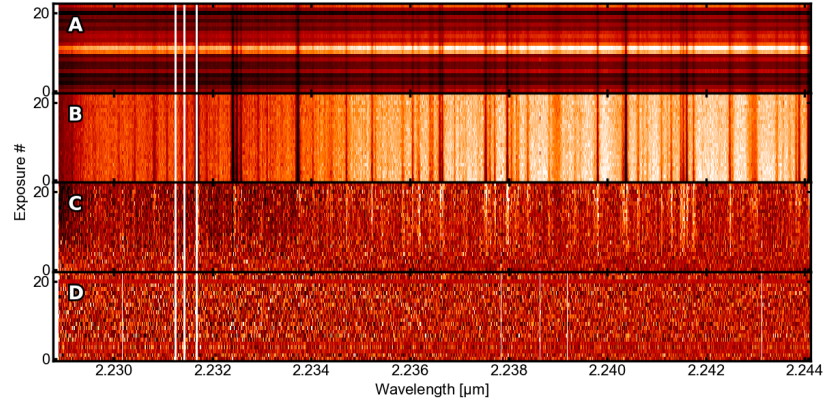
Appendix A: Detrending steps



(a) Example of a reduced HARPS transit time-series gathered on January 5th, 2025.



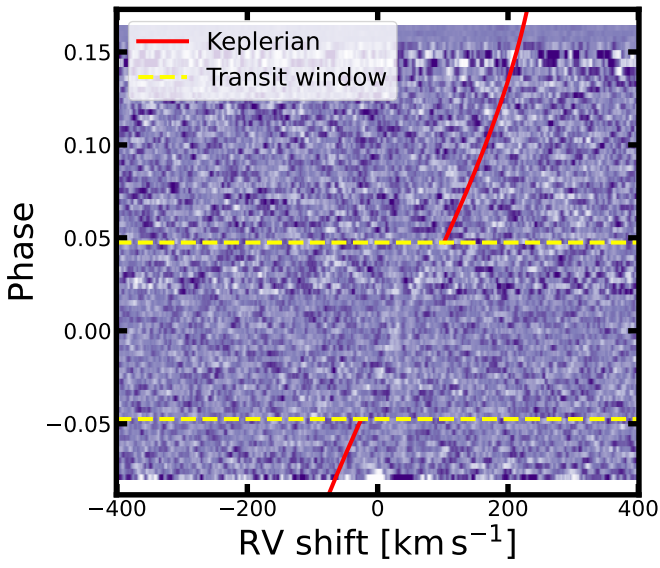
(b) Example of a reduced NIRPS transit time-series gathered on January 5th, 2025.



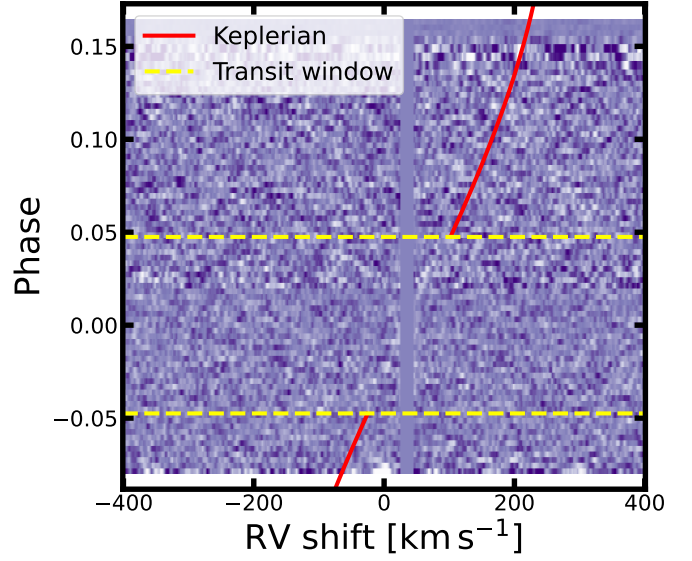
(c) Example of a reduced CRRES+ transit time-series gathered on December 21st, 2021.

Fig. A.1: Data detrending procedure for an example spectral order (exposures versus wavelengths) from HARPS (panel a), NIRPS (panel b), and CRRES+ (panel c). Each panel shows the following steps: A — the raw time-series of a single spectral order during the transit; B — after continuum normalization; C — after dividing out the median out-of-transit spectrum; D — final residuals after removing stellar and telluric spectral lines using PCA.

Appendix B: Correction for stellar effects



(a) HARPS data not masked for the Doppler shadow.



(b) HARPS data masked for the Doppler shadow around the reference systemic velocity ($\approx 38 \text{ km s}^{-1}$).

Fig. B.1: Iron cross-correlation trail maps for HARPS optical data exhibiting non-negligible stellar contamination (i.e. Rossiter–McLaughlin effect) at the systemic velocity expected from [Delrez et al. \(2016\)](#). Dashed yellow lines define the transit window. The solid red line illustrates the Keplerian curve (i.e. the planet’s orbital motion). Panel (a) shows the HARPS optical data not corrected for the stellar contamination as Doppler shadow, while panel (b) shows the Doppler shadow masked (corresponding flux values are set to NaN and discarded).